



저작자표시-비영리-변경금지 2.0 대한민국

이용자는 아래의 조건을 따르는 경우에 한하여 자유롭게

- 이 저작물을 복제, 배포, 전송, 전시, 공연 및 방송할 수 있습니다.

다음과 같은 조건을 따라야 합니다:



저작자표시. 귀하는 원저작자를 표시하여야 합니다.



비영리. 귀하는 이 저작물을 영리 목적으로 이용할 수 없습니다.



변경금지. 귀하는 이 저작물을 개작, 변형 또는 가공할 수 없습니다.

- 귀하는, 이 저작물의 재이용이나 배포의 경우, 이 저작물에 적용된 이용허락조건을 명확하게 나타내어야 합니다.
- 저작권자로부터 별도의 허가를 받으면 이러한 조건들은 적용되지 않습니다.

저작권법에 따른 이용자의 권리는 위의 내용에 의하여 영향을 받지 않습니다.

이것은 [이용허락규약\(Legal Code\)](#)을 이해하기 쉽게 요약한 것입니다.

[Disclaimer](#)

Doctoral Thesis

Maximizing Charge Density of Triboelectric
Nanogenerator based on Design of Dielectric Layer

Jae Won Lee

Department of Materials Science and Engineering

Graduate School of UNIST

2019

Maximizing Charge Density of Triboelectric Nanogenerator based on Design of Dielectric Layer

Jae Won Lee

Department of Materials Science and Engineering

Graduate School of UNIST

Maximizing Charge Density of Triboelectric Nanogenerator based on Design of Dielectric Layer

A thesis/dissertation
submitted to the Graduate School of UNIST
in partial fulfillment of the
requirements for the degree of
Doctor of Philosophy

Jae Won Lee

06. 10. 2019

Approved by



Advisor

Jeong Min Baik

Maximizing Charge Density of Triboelectric Nanogenerator based on Design of Dielectric Layer

Jae Won Lee

This certifies that the thesis/dissertation of Jae Won Lee is approved.

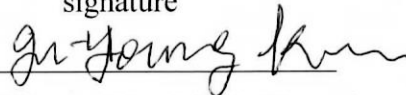
06. 10. 2019

signature



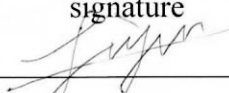
Advisor: Jeong Min Baik

signature



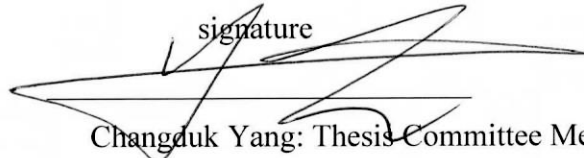
Ju-Young Kim: Thesis Committee Member #1

signature



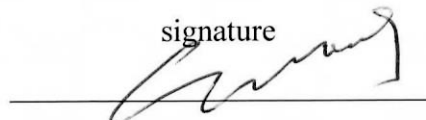
Ji-yun Kim: Thesis Committee Member #2

signature



Changduk Yang: Thesis Committee Member #3

signature



Sang-Woo Kim: Thesis Committee Member #4;

Abstract

Most recently, a newly designed energy generating device named the triboelectric nanogenerator (TENG) was reported and various types of TENGs have been demonstrated, proven as a highly efficient, simple, robust and cost-effective technique for efficiently converting various mechanical energies around us to electricity. In principle, the electrical energy is generated as two different materials are brought into contact with each other, in conjunction with the triboelectric electrification and electrostatic induction. The sources of mechanical energy such as winds and moving things are available anywhere and anytime in our surroundings, thus, TENG will be appropriate as a power-supply unit for portable devices although the energy is not big as expected. Since the first demonstration of the TENG on 2012, various TENG structures and new functional materials brought about the significant increase of the instantaneous power density up to several tens of mW/cm^2 . However, further enhancement is required for faster commercialization, which may be possible by developing functional triboelectric materials, such as dielectrics. First, we set out to design and synthesize Polyvinylidene fluoride (PVDF) graft copolymers to incorporate poly(*tert*-butyl acrylate) (PtBA) through an atom-transfer radical polymerization (ATRP) technique as an efficient dielectric to enhance the output performance of the TENGs. This increase in the dielectric constant significantly increased the density of the charges that can be accumulated on the copolymer during physical contact. The markedly enhanced output performance is quite stable and reliable in harsh mechanical environments due to the high flexibility of the films. Second, we demonstrate high-output TENGs based on polyimide (PI)-based polymers by introducing functionalities (e.g., electron-withdrawing and electron-donating groups) into the backbone. The TENG based on 6FDA-APS PI, possessing the most negative electrostatic potential and the low-lying lowest unoccupied molecular orbital level, produces the highest effective charge density in practical working conditions without the ion injection process. This may be ascribed to the excellent charge-retention characteristics as well as the enhanced charge transfer capability. This article provides a comprehensive review of effective dielectrics used so far in TENG, as well as the fundamental issues regarding the materials. Finally, we show some strategies for obtaining the properties that the materials should have as effective dielectrics.

Contents

CHAPTER 1. INTRODUCTION	1
CHAPTER 2. THEORETICAL BACKGROUND AND MOTIVATION	4
2.1 Triboelectricity	4
2.2 Effect of the work function on electron transfer.....	4
2.3 Triboelectric energy harvesting	5
CHAPTER 3. STRATEGIES FOR EFFECTIVE DIELECTRICS	8
3.1 Importance of dielectric in triboelectric nanogenerator.....	8
3.2 Surface roughening.....	8
3.3 Surface modification	9
3.4 Dielectric constant	10
3.5 Compressibility	11
3.6 References	12
CHAPTER 4. PVDF GRAGTED PtBA COPOLYMERS	14
4.1 Introduction	14
4.2 Experimental details	15
4.2.1 Materials and Instruments	15
4.2.2 Synthesis of PVDF-Gn graft copolymers.....	16
4.2.3 Production of PVDF-based triboelectric nanogenerator.....	16
4.2.4 Characterization and measurements	16
4.3 Results and Discussion	17
4.3.1 Synthesis of PVDF-Gn graft copolymers	17
4.3.2 Fabrication of PVDF-Gn based TENGs and its output performance	18

4.3.3 Mechanical stability and durability of PVDF-Gn based TENG.....	24
4.3.4 AFM, SEM, and Nanoindentation test for the PVDF-Gn films	24
4.3.5 Dielectric properties for PVDF-Gn films	26
4.3.6 Relationship between the dielectric constant and output performance.....	27
4.3.7 Surface potential and UPS measurement of PVDF-Gn films.....	28
4.3.8 XRD pattern of PVDF-Gn films.....	30
4.3.9 Output performance depending on the poling electric field direction	30
4.4 Conclusion	32
4.5 References	34
CHAPTER 5. FLUORINATED PI BASED POLYMERS	36
5.1 Introduction	36
5.2 Experimental details	37
5.2.1 Materials	37
5.2.2 Synthesis of Fluorinated PI through step polymerization.....	38
5.2.3 Fabrication of Fluorinated PI -based triboelectric nanogenerator	38
5.2.4 Materials characterization and TENG performances	39
5.2.5 Fabrication of Gas sensor network systems	40
5.3 Results and Discussion	40
5.3.1 Synthesis of PI-based polymers.....	40
5.3.2 Fabrication of PI based TENGs and its output performance	42
5.3.3 Charge density property of PI based TENGs	46
5.3.4 Electrostatic potential maps of the fluorinated PIs	47
5.3.5 DFT calculation	48

5.3.6 Energy levels of PI-based films.....	49
5.3.7 Sensor network system driven by a TENG	51
5.4 Conclusion	57
5.5 References	58
CURRICULUM VITAE	61

LIST OF FIGURES

- Figure 1.** A list that ranks various materials according to their tendency to gain or lose electrons in contact electrification, called as the triboelectric series.
- Figure 2.** Electron potential energy. (a) metal–metal contact and (b) insulator-insulator contact.
- Figure 3.** Schematic diagrams that illustrate the operating principle of the generator. (a) Open-circuit condition. (b) Short-circuit condition.
- Figure 4.** The process of output power density and current of triboelectric nanogenerators.
- Figure 5.** (a) Synthesis of PVDF-Gn graft copolymers and photograph of the PVDF and PVDF-G18 NMP solutions, respectively. (b) ¹H NMR, (c) FT-IR of PVDF and PVDF-Gn.
- Figure 6.** (a) Schematic diagrams of the fabrication process for the PVDF-Gn based TENGs. (b) Photographs of a flexible PVDF-Gn film after peeled off and a PVDF-Gn based TENG. (c) The output current densities generated by the PVDF-based TENGs as a function of the PtBA mole percent ranging from 0 to 18%. (d) The output voltages, current densities, and the output power densities of the PVDF-G18 based TENG with the resistance of external loads from 1 to 10⁹ Ω. (e) Charge densities generated by the PVDF-based TENGs as a function of the PtBA mole percent ranging from 0 to 18%. (f) The measured voltage of a commercial capacitor (1, 2.2, 3.3, 10, 22, 33, 100, 220, 330, 1000 μF) charged with AC to DC signal converting circuit by using PVDF-G18 based TENG.
- Figure 7.** The output voltages generated by the PVDF-based TENGs as a function of the PtBA mole percent ranging from 0 to 18%.
- Figure 8.** (a) The output voltages generated by the different polymer based TENGs. (b) The output current densities generated by the different polymer based TENGs.
- Figure 9.** (a) The output voltages generated by the different polymer based TENGs. (b) The output current densities generated by the different polymer based TENGs.
- Figure 10.** Average current density and charge density generated by the PVDF-G15 and -G18 based TENG. Error bars represent standard error of the mean (S.E.M.).

Figure 11. The calculated electrostatic potentials inside the nanogenerator with PtBA mole percents ranging from 0 to 18%.

Figure 12. (a) Optical images of the portable power-supplying system with AC to DC converting circuit and (b) The measured voltage of a commercial capacitor (1, 2.2, 3.3, 10, 22, 33, 100, 220, 330, 1000 μ F) charged with AC to DC signal converting circuit by using pristine PVDF based TENG.

Figure 13. (a) Mechanical bending tests of the PVDF-based TENG. (b) The output current densities generated by the pristine PVDF-based and the PVDF-G18 based TENGs before and after bending 3,000 times. (c) Stability and durability test of the TENG under cycled compressive force of 50 N over 18,000 cycles.

Figure 14. (a) 3-dimensional AFM images and (b) Cross-sectional SEM images for PVDF-based films with various PtBA mole percent ranging from 0 to 18%.

Figure 15. (a) The loading and unloading curves measured by nanoindentation test for the PVDF-Gn film of the mole percents (0, 10, 15, and 18%) of PtBA. (b) The elastic modulus and hardness of PVDF-Gn films of the mole percents (0, 10, 15, and 18%) of PtBA. Error bars represent standard error of the mean (S.E.M.).

Figure 16. Frequency dependence of (a) dielectric constant values and (b) loss tangent for PVDF-based films with various PtBA mole percent ranging from 0 to 18%.

Figure 17. The dielectric constant of PVDF-Gn films according to the mole percent (0, 10, 15, and 18%) of PtBA. Error bars represent standard error of the mean (S.E.M.).

Figure 18. (a) Measured output currents of the PVDF-based TENG with the grafting ratio. (b) Saturated time and output current as a function of the PtBA mole percent ranging from 0 to 18%. Error bars represent standard error of the mean (S.E.M.). (c) Calculated charging time of the capacitor increases from 2.3 sec to 4.52 sec with the increase of the dielectric constant.

Figure 19. (a) KPFM surface potential distribution images ($3 \mu\text{m} \times 3 \mu\text{m}$) of Au, pristine PVDF, and PVDF-G18 films. (b) The work function values of pristine PVDF and PVDF-G18 films, obtained from the KPFM results. (c) UPS spectra and (d) the change in work function of Al, pristine PVDF, and PVDF-G18 film. Error bars represent

standard error of the mean (S.E.M.).

Figure 20. (a) The high-resolution XRD patterns of pristine PVDF and PVDF-Gn films as a function of PtBA mole percent. (b) The expanded view of the 2nd peak in Figure 20a. The peak can be deconvoluted into two peaks, α (110) (red) and β (200) phase (blue).

Figure 21. Structures of PVDF and PVDF-Gn.

Figure 22. The output voltages and current densities for (a) pristine PVDF and (b) PVDF-G18 based TENGs under different poling electric fields direction. (c) Circuit diagrams and the different performances among TENGs fabricated using different poling electric field direction.

Figure 23. Scheme for the synthesis of polyimides (6FDA-ODA, 6FDA-PDA, and 6FDA-APS) by a two-step method.

Figure 24. (a) Structures and ¹H NMR spectra of the PI-based Polymers: 6FDA-ODA; 6FDA-PDA; 6FDA-APS. The inset shows ¹H NMR spectra of the PAAs. FT-IR spectra of (b) PAAs and (c) PIs.

Figure 25. FT-IR spectra of (a) PAAs and (b) PIs: 6FDA-ODA; 6FDA-PDA; 6FDA-APS.

Figure 26. (a) Schematic diagrams of the fabrication process for the PI-based TENGs. (b) Photographs on the left side with scale bars of 1 cm and cross-sectional scanning electron microscope (SEM) images in centre with scale bars of 50 μ m of the fluorinated PIs: 6FDA-ODA; 6FDA-PDA; 6FDA-APS. The photograph of the PI-based TENG (consisting of 6FDA-APS film and stretchable electrode) is also shown in right side. Scale bar, 1 cm. (c) The V_{oc} and J_{sc} of the TENGs with different polymers: Kapton; 6FDA-ODA PI; 6FDA-PDA PI; 6FDA-APS PI. (d) The instantaneous power of the PI-based TENG with external loads ranging from 1 M Ω to 20 M Ω . (e) Instantaneous output voltage, current, and power of TENG were measured under 5 M Ω . The generated energy of about 0.1 mW under a frequency of 3 Hz. (f) The instantaneous power and average power (μ J/s) of the TENGs with different polymers. The inset shows the generated energy per peak.

Figure 27. The output current and voltage of the PI-based TENG with an external load ranging from 1 M Ω to 20 M Ω .

Figure 28. Instantaneous output voltage and current of TENGs with different polymers were measured under 5 M Ω .

Figure 29. The (a) J_{sc} and (b) V_{oc} of the TENGs with PTFE and 6FDA-APS PI. (c) The instantaneous power of the PTFE-based TENG with an external load ranging from 1 M Ω to 20 M Ω . (d) Charge densities generated by the TENGs with PTFE.

Figure 30. (a) Charge densities generated by the TENGs with different polymers: Kapton; 6FDA-ODA PI; 6FDA-PDA PI; 6FDA-APS PI. The charge densities with the PI-based films as a function of (b) the input frequencies ranging from 0.05 to 10 Hz and (c) the mean free times between the contacts ranging from 0.1 to 19.1 sec.

Figure 31. Electrostatic potential maps of the fluorinated PIs: 6FDA-ODA; 6FDA-PDA; 6FDA-APS.

Figure 32. (a) Energy diagram of three monomers, of which energy levels are aligned with respect to vacuum energy level, between LUMO and LUMO+5. (b) Electrostatic planar average potentials and the corresponding energy barrier heights for electron transfer from Al electrode to monomers. (c) The output powers of the PI-based TENGs with barrier height and LUMO level.

Figure 33. (a) Cyclic voltammetry of the fluorinated PIs: 6FDA-ODA; 6FDA-PDA; 6FDA-APS. (b) UV-vis absorption spectra in the range from 300 to 800 nm. (c) Corresponding plot of transformed Kubelka–Munk function versus the energy of the light.

Figure 34. (a) Schematic diagrams and the photograph of the 6FDA-APS PI film-based three-layered TENG. (b) Charge densities generated by the TENG fabricated with PTFE film and 6FDA-APS PI film.

Figure 35. (a) Schematic diagram of the gas sensor network system driven by the 6FDA-APS PI film-based TENG. (b) The charging curves of the 10- μ F capacitor by the TENG before and after NO₂ exposure as a function of input frequencies and the corresponding change in currents changes of 4 sensors with the NO₂. (c) The change in currents of each sensor toward the three gases (H₂, CO, and NO₂) as a function of gas concentration from 1 ppm to 100 ppm, measured at 250°C. (d)

Principal component analysis, plotted as three-dimensional maps. (e) Conceptual schematic diagram of the self-powered sensor network systems. (f) The photographs of the lit LEDs; Yellow (H_2), Red (NO_2), and Green (CO).

Figure 36. (a) Size distribution via dynamic light scattering (DLS) for ZnO and SnO₂ nanoparticles. (b) SEM images of ZnO and SnO₂ nanoparticles with scale bars of 100 nm. (c) X-ray diffraction (XRD) patterns of ZnO and SnO₂ nanoparticles.

Figure 37. Flow chart of the gas identity algorithm.

Figure 38. Systematic configuration of the self-powered sensor network system.

Figure 39. The captured images from Supplementary movie 1, 2, and 3 showing the H_2 , NO_2 , and CO gas identification of sensor network system.

CHAPTER 1. INTRODUCTION

Energy is one of the most important resources that determines the quality of human life. The fossil energy is in danger of running out before long and energy consumption, in particular, has been increasing exponentially, one year after the other. Thus, the search for renewable energy sources remains one of the most important ongoing endeavors of our age. So far, the most favorable energy sources have been considered to be solar, wind, and tidal energy. Actually, such energy sources generated mega- to giga-watt power for industrial applications, in which the energy harvesting technologies should be low cost, high stability, and high efficiency.¹

In the last two decades, the various applications of mobile electronics such as smart phone and smart watch are big part of our lives. The mobile devices have various functionalities such as health monitoring, medical care, environmental protection, infrastructure monitoring and security. This means that there were so many devices to power up for operating them although the power for driving each unit is small and can be down to milli to micro-watt range. The recent development of internet of things and sensor networks dramatically change the existing understanding about energy, which should be mobile, available, and sustainable nowadays. This is why we are using batteries per every devices. However, it may not be the solution because so many batteries are needed and they have a limited life time. Thus, we have to monitor and exchange them, which is an impossible task and costs a great deal. It is essential to develop portable power generating device which provides energy with the battery for a self-powered system.²

A new energy generating device, triboelectric nanogenerators (TENGs) uses the mechanical energy sources available anywhere and anytime at our surroundings, such as winds, ocean waves, and moving things. The wind energy, as an alternative candidate to fossil fuels, is plentiful, renewable, widely distributed, and clean, and produces no air pollution during operation.³ Due to these advantages, yearly wind energy production by using many individual wind turbines is also growing rapidly and has reached around 4 % of worldwide electric power usage. Wave energy is originated from the transport of energy by wind waves at the ocean.⁴ Although it has a lot of advantages, it is not currently a widely employed commercial technology. The energy harvester from moving things may be appropriate for the portable applications although the energy is not big as much as the solar energy.⁵

Generally, different materials have different affinities for electrons. By rubbing a variety of materials against each other and seeing the charge transfer between them, the materials can be

ordered according to their affinity for electron, called as triboelectric series. One such ordering for several materials is shown in Figure 1.⁶ Materials shown highest (left) on the figure tend to have a greater affinity for electrons than those below it (right). Subsequently, when any two materials in the figure are rubbed together, the one that is higher can be expected to attract electrons from the material that is lower. As such, the materials accepting the electrons have the greatest tendency to acquire the negative charge, while those losing the electrons become positively charged. In general, the stable atoms have greater electron affinity, for example, most electron-withdrawing polymers contain elements with strong electron affinity, such as fluorine (F). Thus, by introducing additional F atoms onto the polymer, by chemically grafting F-containing unit, such as CF₃ group, the charge density transferred is expected to increase.


Positive 	Polyurethane foam	(continued)	 Negative
	Etylcellulose	Polyester (Dacron)	
	Sorbothane	Polyisobutylene	
	Polyamide 6-6	Polyuretane flexible sponge	
	Hair, oily skin	Polyethylene Terephthalate (PET)	
	Wool, Knitted	Polyvinyl butyral	
	Silk, woven	Polychlorobutadiene	
	Aluminum	Natural rubber	
	Paper	Polyacrilonitrile	
	Cotton, woven	Polystyrene	
	Steel	Polyimide	
	Wood	Neoprene	
	Hard rubber	Polyehylene	
	Nickel, copper	Polypropylene	
	Sulfur	Polyimide (Kapton)	
	Brass, silver	Polyvinyl chloride (PVC)	
	Acetate, Rayon	Latex (natural) rubber	
	Polymethyl methacrylate (Lucite)	Santoprene rubber	
	Polyvinyl alcohol	Polydimethylsiloxane (PDMS)	
	(continued)	Polytetrafluoroethylene (Teflon)	

Figure 1. A list that ranks various materials according to their tendency to gain or lose electrons in contact electrification, called as the triboelectric series.

Following the principal that grafting one polymer onto another polymer backbone can combine the benefits of each parent polymer, we set out to design and synthesize PVDF graft copolymers to incorporate poly(*tert*-butyl acrylate) (PtBA) through an atom transfer radical polymerization (ATRP) technique, as an efficient dielectric to enhance the output performance

of the TENGs. The grafting of PtBA onto the PVDF backbone suppressed the formation of the β phases; hence, the PVDF-Gn graft copolymers were mainly composed of the α phases. As the grafting ratio increased to 18 %, the dielectric constant values increased from 8.6 to 16.5 in the frequency range of $10^2 - 10^5$ Hz, which were attributed to the increase of the net dipole moment of the materials, supported by the Kelvin probe force microscopy measurements (KPFM). The TENG fabricated with the graft copolymer generated the output voltage and current density of 64.4 V and $18.9 \mu\text{A}/\text{cm}^2$, twice the enhancement in both, compared to pristine PVDF based TENG. Further increase in the output performance to 105 V and $25 \mu\text{A}/\text{cm}^2$, 20 times enhancement in output power, was also obtained by tuning the surface potential via poling method, which improved the charges accepting characteristics. The enhanced output performance was quite stable and reliable under harsh mechanical environment due to the high flexibility of the film. A much faster charging property was also demonstrated in this study.

In the work described herein, we synthesize polyimide (PI)-based polymers (6FDA-ODA, 6FDA-PDA, and 6FDA-APS) by introducing functionalities (e.g., electron-withdrawing and electron-donating groups) into the backbone. Among them, the TENG based on 6FDA-APS PI, possessing the most negative electrostatic potential and the low-lying lowest unoccupied molecular orbital (LUMO) level, showed superior performances. (i) Its charge density increased by about 7 times compared with that of the commercially available PI (Kapton) film-based one; (ii) Its maximum effective charge density of about $512 \mu\text{C}/\text{m}^2$ under 3 Hz, the highest charge density of TENGs in practical working conditions to the best our knowledge, was obtained without the artificial ion injection process; (iii) Measurement of frequency-dependent output currents showed that its charge density was the largest over the entire frequency range, indicating the best charge-retention characteristics as well as enhanced charge transfer capability of 6FDA-ODA PI; (iv) In addition, a 6FDA-APS-driven sensor network system was also demonstrated, providing the identity of the gases (H_2 , CO, and NO_2) by turning on light-emitting diodes (LEDs) within several seconds.

CHAPTER 2. THEORETICAL BACKGROUND AND MOTIVATION

2.1 Triboelectricity

Triboelectricity is characterized by a number of regularities. When friction occurs between two chemically identical bodies, the denser body is positively charged. When there is friction between a metal and a dielectric, the metal may be electrified with either positive or negative polarity. When friction occurs between two dielectrics, the dielectric with the higher dielectric constant ϵ is positively charged.⁷ Triboelectricity in solids is attributed to the transfer of charge carriers from one body to the other. In the cases of two metals, two semiconductors, or a metal and a semiconductor, triboelectricity is caused by the transfer of electrons from the substance with the lower work function to the substance with the higher work function. When two different materials are brought into contact and separated, an electric charge is transferred from one to the other.⁷

2.2 Effect of the work function on electron transfer

Charge generated by triboelectrification between materials in contact and separation is a prime cause of triboelectricity. The charge transfer is explained in terms of ‘electron transfer’ arising from the difference in work function between the surfaces. If two metals of different work functions are placed in contact, the Fermi levels of the two metals will coincide and this will result in a potential difference being established between the adjacent faces of the two samples. Two metals with different work functions ϕ_1 and ϕ_2 in contact are schematically shown in Figure 2. Assuming that electron transfer takes place by tunneling so that thermodynamic equilibrium prevails, the contact potential difference V_c is given by

$$V_c = V_{1/2} = -\frac{(\phi_1 - \phi_2)}{e} \quad (1)$$

where $V_{1/2}$ is the contact potential difference of metal 1 against metal 2, e is the elementary charge. The amount of the transferred charge is equal to the product of the contact potential difference and the capacitance between the two bodies. The capacitance depends on the state of the contacting surfaces. Although the position of the electrons can vary after the metals are separated, the net charge transferred Δq_c is approximated by the following equation:

$$\Delta q_c = C_0 V_c \quad (2)$$

where C_0 is the capacitance between the bodies at the critical separation distance where the charge transfer is cutoff. The difference is probably caused by uncertain factors, such as surface roughness, impurities, oxidized layer, separation speed, and others.

When the insulators come to contact, electrons move from the filled surface states of insulator 1 to the empty surface states of insulator 2. The driving force for the charge transfer between the surfaces is the difference in the effective work functions of the two surfaces.⁸

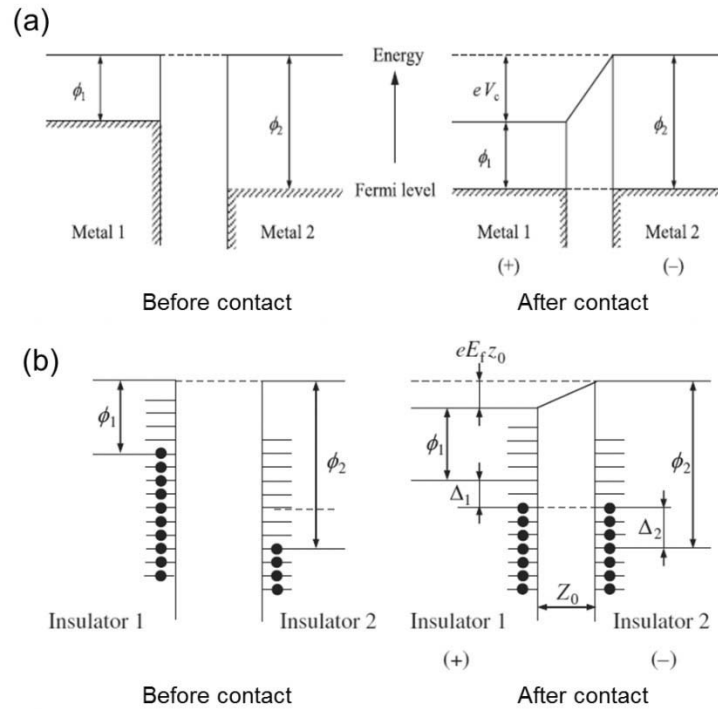


Figure 2. Electron potential energy. (a) metal–metal contact and (b) insulator-insulator contact.

2.3 Triboelectric energy harvesting

Traditional TENG is a mechanical device that produces static electricity or electricity at high voltage by contact charging. The most popular ones are the Wimshurst machine and Van de Graaff generator, which were invented in ~1880 and 1929, respectively. Both machines use the accumulated static charges generated by triboelectrification; the tribo-charges are transferred from a rotating belt to a metal brush by the corona discharging (*e.g.*, the electric-field-induced arching of air); once the accumulated charge density reaches a critical value, discharging over two opposite electrodes occurs. It appears that the traditional TENG is a high voltage source, and there is no current unless there is a discharging.

However, in early 2012, this phenomenon systematically studied and found that it was a triboelectrification-driven energy conversion process.⁹ This was the birth of the TENG, which is distinctly different from the traditional Van de Graaff generator in a way that electrostatic induction is introduced for output power. The operating principle of the TENG for the case of dielectric-to-dielectric in contact mode can be described by the coupling of contact charging and electrostatic induction.¹⁰

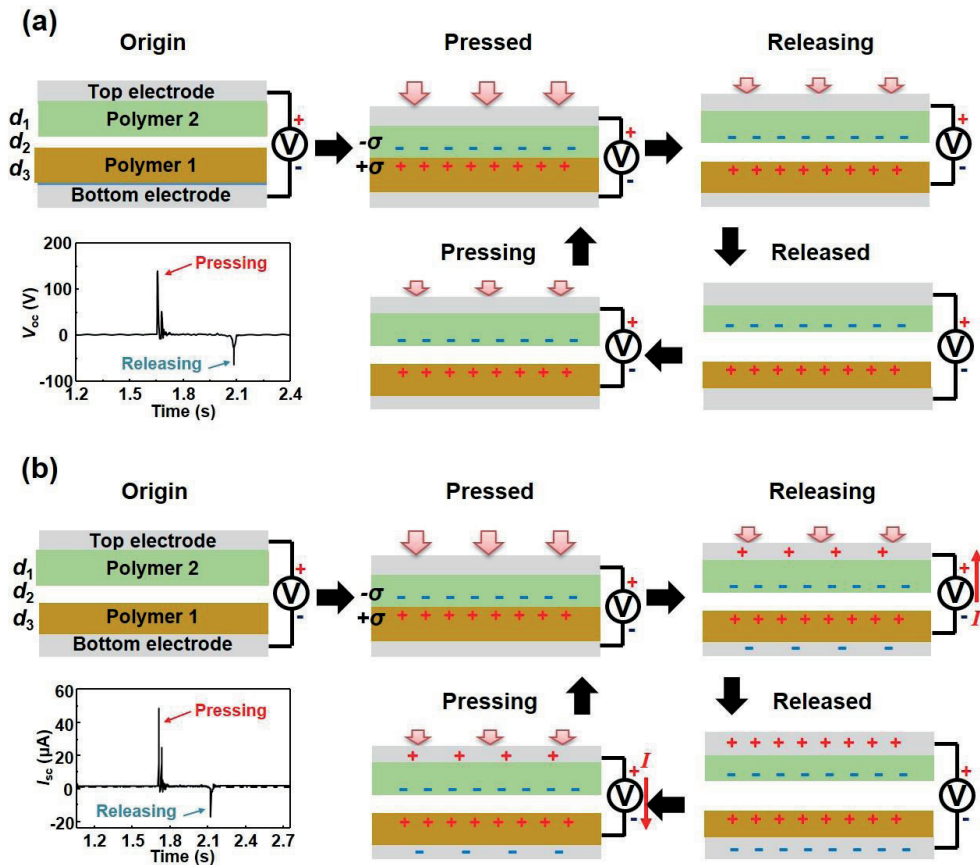


Figure 3. Schematic diagrams that illustrate the operating principle of the generator. (a) Open-circuit condition. (b) Short-circuit condition.

Figure 3a and 3b show the electric output of open-circuit voltage and short-circuit current. In the original state, no charge is generated or induced, with no electric potential difference (EPD) between the two electrodes. With an externally applied force, the two polymers are brought into contact with each other. Surface charge transfer then takes place at the contact area due to triboelectrification. According to the triboelectric series, which is a list of materials based on their tendency to gain or lose charges, electrons are injected from polymer 1 into polymer 2, resulting in net negative charges at the polymer 2 surface and net positive

charges at the polymer 1 surface, respectively. It is worth noting that the insulating property of the polymers allows a long-time retention of triboelectric charges for hours or even days. Since they are only confined on the surface, charges with opposite signs coincide at almost the same plane, generating practically no EPD between the two electrodes.

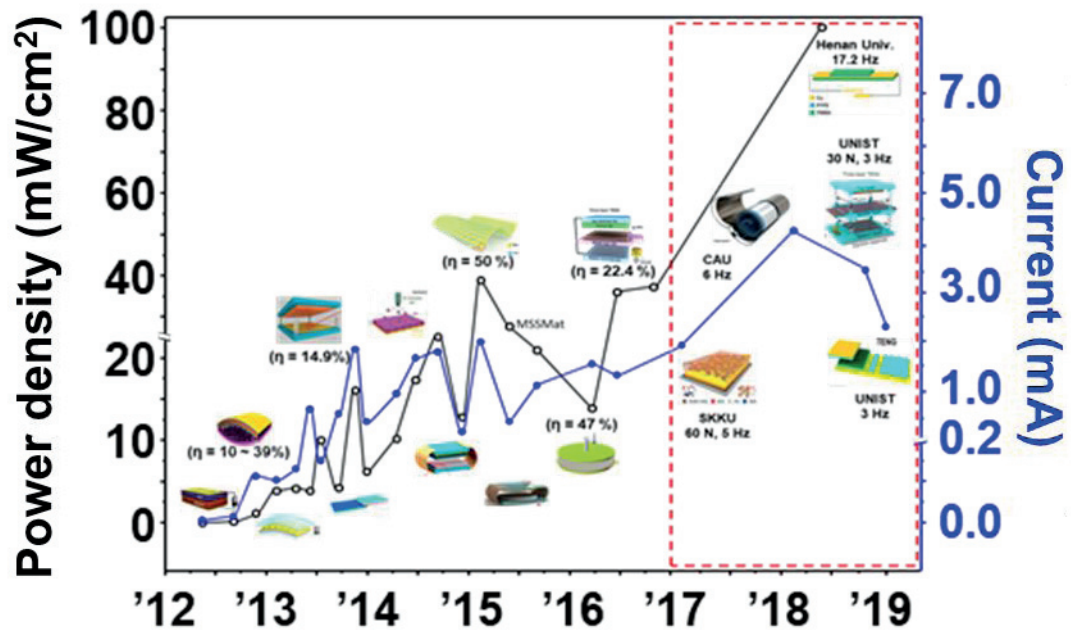


Figure 4. The process of output power density and current of triboelectric nanogenerators.

CHAPTER 3. STRATEGIES FOR EFFECTIVE DIELECTRICS

3.1 Importance of dielectric in triboelectric nanogenerator

The output performance of the TENG has been significantly increased during last 4 ~ 5 years and the instantaneous areal power density has reached up to several tens of mW/cm². However, the increase of the output power does not mean the increase of the energy conversion efficiency. It tells us facts that the fabricated TENGs can generate the output powers at certain input conditions (*i.e.* large input force or optimized input condition). The areal output currents reported are also still less than 1 mA/cm², too low to provide enough energy with electronic devices. Actually, it is so hard to charge the smartphone/smartwatch battery above 1 % with the TENGs. Recently, it seems that there are no longer significant increase in the output current. Most of works has focused on the optimization of the device structures as well as the demonstration of new applications. Although the strategies were quite successful and many potential applications were reported, it is essential to develop a breakthrough technology for the further enhancement in output performance to speed up the commercialization of the TENG. We will approach the technology from a new viewpoint, materials aspect.

In most TENGs, the two materials were chosen according to the triboelectric series and charges are transferred from one to the other material during the contact. Thus, a key approach to improve the output performance of the TENGs from the materials aspect is to increase the triboelectric surface charge. Thus, the commercialization of the TENGs would be possible only if there are effective dielectrics because the output power is critically and basically dependent on the density of the charges transferred.^{11,12} So far, various dielectric materials such as polydimethylsiloxane (PDMS),¹³ polytetrafluoroethylene (PTFE),¹⁴ polyvinylidene fluoride (PVDF),¹⁵ fluorinated ethylene propylene (FEP),¹⁶ polyimide (PI),¹⁷ have been used without any modifications. Very recently, the modification of properties such as compressibility,¹¹ surface potential,¹⁸ and hydrophobicity¹⁹ in a few TENGs have been reported.

3.2 Surface roughening

To increase the output power of TENG, the easiest and most effective way is to increase the surface-to-volume ratio of two contact materials. So far, various morphologies like NWs, NPs or other nanoscale patterns were frequently adopted, thus made more charge carrying site. A simple etching method was usually used to make such nanostructures. The fluorocarbon

plasma treatment could make a PDMS film of wrinkled surface, caused by the velocity from the fluorocarbon polymer and different surface tension between the PDMS and the fluorocarbon polymer layer, with chemically modified surfaces.²⁰ For the PDMS, various Si molds such as lines, cubes, and pyramid, were used to make some patterns on the PDMS surfaces.²¹ The liquid PDMS elastomer and cross-linker were mixed, degassed, and uniformly coated on the surface of the master mold.²² After curing process, the films were peeled-off and attached on the conducting substrates to fabricate the TENG. Block copolymer self-assembly, by the microscopic phase separation of covalently linked polymer blocks, was also used for achieving densely arranged nanoscale patterns including dots, lines, holes, and rings. These methods were quite effective in increasing the effective contact area to generate more triboelectric charges.

3.3 Surface modification

As mentioned above, the operation of TENGs is based on the combined effects of triboelectrification and electrostatic induction occurring on both surfaces. The magnitude of the electrons flowing through the external circuit is strongly influenced by how many charges are transferred to the dielectric. The charge density transferred is closely related to the chemical properties of both surfaces, thus, the surface modification by appropriate functionalization methods is effective in increasing the charge density. In general, the transferred charge density (σ) on the surface of the dielectric is explained as,¹¹

$$\sigma = \frac{[(W-E_0)/e](1+t/\varepsilon z)}{t/\varepsilon\varepsilon_0 + (1/\overline{N_s(E)}e^2)(1+t/\varepsilon z)} \quad (3)$$

where $W-E_0$ is the difference in the effective work functions between two materials, e , t , ε , ε_0 , z , and $\overline{N_s(E)}$ are the charge of an electron, distance of space, relative permittivity of dielectric, vacuum permittivity of free space, depth of dielectric film, and the averaged surface density of states. This shows that as the work function difference of two contact materials increases, the surface charge density also increases. According to this equation, most of works on the surface modification of the dielectric has focused on the control of the surface potentials.

The chemical potential of organic materials is mainly determined by its functional groups exposed on the surface. As mentioned above, of functional groups, fluoro ($-F$) has the highest tendency to attract electrons. A perfluorinated molecules containing only carbon-

fluorine (C–F bonds) and C–C bonds such as PTFE are known as the most triboelectrically negative choices.

3.4 Dielectric constant

Dielectric constant of the dielectric is one of important parameters in determining the charge density transferred, thus, the output performance of the TENG. This parameter may be related with the maximum magnitude of the charges that can be sustained on the surface and inside the bulk. The surface modifications mentioned above will increase the density of charges on the surface, not inside the bulk. In general, the total transferred charge density (σ') can be expressed by,²³

$$\sigma' = \frac{-\sigma_0 d_{gap}}{d_{gap} + d_{dielectric} / \epsilon_{dielectric}} \quad (4)$$

where σ_0 is the triboelectric charge density at the equilibrium state, d_{gap} and $d_{dielectric}$ are the gap distance and the thickness of dielectric films, and $\epsilon_{dielectric}$ is a dielectric constant of dielectric films. According to the above equation, the charge density can increase as the dielectric constant increases.

One of the facile methods to increase the dielectric constant of the dielectric film is to make composites, composed of inorganic and organic materials. A composite composed of a barium titanate (BaTiO₃) NPs and a ferroelectric copolymer matrix, poly(vinylidene fluoride-co-trifluoroethylene) (P(VDF-TrFE)) was reported.²⁴ The insertion of the BaTiO₃ into the P(VDF-TrFE), followed by the poling process, increased the dielectric constant from 10.9 to 12.4 at 10² Hz. This may be due to the high dielectric properties of the BaTiO₃. The TENG fabricated with this film show approximately 5 times enhancement in output current, ~0.3 mA. It was concluded that BaTiO₃ NPs played an important role in obtaining such a large output current by increasing the electrical charge-trapping capability of the TENG. Similarly, the PDMS film consisting of 10% SrTiO₃ NPs in volume showed the excellent performance, where the output open-circuit voltage, short-current density, and transfer charge increased up to 338 V, 9.06 $\mu\text{A cm}^{-2}$, and 19 nC/cm², respectively.¹² The maximum instantaneous output power is 6.47 W/m² under periodic compressive force at frequency of 2.5 Hz.

3.5 Compressibility

In addition to the dielectric constant, the compressibility of the film is so important because the TENG is based on the dynamic motion. This means that the charge density transferred is influenced by the mechanical properties of the film. In metal/dielectric/metal structure, the charge density is expressed by $Q = CV$. A first derivative of charges with respect to time is as follows;

$$\frac{dQ}{dt} = \frac{dC}{dt}V + C \frac{dV}{dt} \quad (5)$$

This equation can tell us that the rate of capacitance with the time is also an important parameter as well as the dielectric constant. As a simple method to increase the rate, a mesoporous film was fabricated by using polystyrene (PS) spheres as a sacrificial template.²⁵ First, many layers of PS spheres were coated on a SiO₂/Si substrate and PDMS solution was poured into periodically arranged PS spheres, and an amorphous free-standing film was formed by heating on a hot plate at 90°C. After the removal of the PS, the PDMS inverse opal structured film was fabricated. The TENGs showed a 10-fold power enhancement compared with those with flat film. They showed that the enhancement was due to the increase of the contact area and the capacitance by the increase in effective (ϵ/d) value. This film was also less sensitive to humidity and produced stable output power. A mesoporous PDMS film impregnated with Au NPs as effective dielectrics was also reported by same group.²⁶ This film was fabricated by casting a mixture of PDMS solution and DI water, evaporating water very slowly at room temperature. The Au NPs were accumulated only at the bottom side of the pores, which generated the electric potential by the friction between the Au NPs and PDMS. The porosity could be controlled by the content of the water in the mixture and increased with the content. They also showed that a large-area mesoporous PDMS thin film (30 cm × 30 cm) could be fabricated, demonstrating the capability of producing large-scale films. Due to the larger porosity of the films, it was clearly seen that the mesoporous film became quite compressible and flexible.

3.6 References

- 1 Z. L. Wang, J. Chena and L. Lina, *Energy Environ. Sci.*, 2015, **8**, 2250–2282.
- 2 Z. L. Wang, *Sci. Am.*, 2008, **298**, 82.
- 3 J. Bae, J. Lee, S. Kim, J. Ha, B.-S. Lee, Y. Park, C. Choong, J.-B. Kim, Z. L. Wang, H.-Y. Kim, J.-J. Park and U.-I. Chung, *Nat. Commun.*, 2014, **5**, 4929.
- 4 G. Zhu, Y. Su, P. Bai, J. Chen, Q. Jing, W. Yang and Z. L. Wang, *ACS Nano*, 2014, **8**, 6031-6037.
- 5 K. N. Kim, J. P. Lee, S-H. Lee, S. C. Lee and J. M. Baik, *RSC Adv.*, 2016, **6**, 88526–88530.
- 6 A. F. Diaz and R. M. Felix-Navarro, *J. Electrostat.*, 2004, **62**, 277–332.
- 7 Triboelectric. (n.d.) McGraw-Hill Dictionary of Scientific & Technical Terms, 6E. (2003). Retrieved July 9 2019 from <https://encyclopedia2.thefreedictionary.com>
- 8 S. Matsusaka, H. Maruyama, T. Matsuyama, M. Ghadiri, *Chem. Eng. Sci.*, 2010, **65**, 5781–5807.
- 9 F.-R. Fan, Z.-Q. Tian and Z. L. Wang, *Nano Energy*, 2012, **1**, 328–334.
- 10 G. Zhu, C. F. Pan, W. X. Guo, C. Y. Chen, Y. S. Zhou, R. M. Yu and Z. L. Wang, *Nano Lett.* 2012, **12**, 4960–4965.
- 11 J. Chun, B. U. Ye, J. W. Lee, D. Choi, C.-Y. Kang, S.-W. Kim, Z. L. Wang and J. M. Baik, *Nat. Commun.*, 2016, **7**, 12985.
- 12 J. Chen, H. Guo, X. He, G. Liu, Y. Xi, H. Shi and C. Hu, *ACS Appl. Mater. Interfaces*, 2016, **8**, 736–744.
- 13 G. Zhu, Z.-H Lin, Q. Jing, P. Bai, C. Pan, Y. Yang, Y. Zhou and Z. L. Wang, *Nano Lett.*, 2013, **13**, 847–853.
- 14 P. Bai, G. Zhu, Z.-H. Lin, Q. Jing, J. Chen, G. Zhang, J. Ma, and Z. L. Wang, *ACS Nano*, 2013, **7**, 3713–3719.
- 15 P. Bai, G. Zhu, Y. S. Zhou, S. Wang, J. Ma, G. Zhang and Z. L. Wang, *Nano Res.*, 2014, **7**, 990–997.
- 16 P. Bai, G. Zhu, Q. Jing, J. Yang, J. Chen, Y. Su, J. Ma, G. Zhang and Z. L. Wang, *Adv. Funct. Mater.*, 2014, **24**, 5807–5813.
- 17 Z. Zhao, X. Pu, C. Du, L. Li, C. Jiang, W. Hu and Z. L. Wang, *ACS Nano*, 2016, **10**, 1780–1787.
- 18 Y. S. Zhou, S. Wang, Y. Yang, G. Zhu, S. Niu, Z.-H. Lin, Y. Liu and Z. L. Wang, *Nano Lett.*, 2014, **14**, 1567–1572.

- 19 S. Wang, Y. Xie, S. Niu, L. Lin, C. Liu, Y. S. Zhou and Z. L. Wang, *Adv. Mater.*, 2014, **26**, 6720–6728.
- 20 X. Cheng, B. Meng, X. Chen, M. Han, H. Chen, Z. Su, M. Shi and H. Zhang, *Small*, 2016, **12**, 229–236.
- 21 X.-S. Zhang, M.-D. Han, R.-X. Wang, F.-Y. Zhu, Z.-H. Li, W. Wang and H.-X. Zhang, *Nano Lett.*, 2013, **13**, 1168–1172.
- 22 C. K. Jeong, K. M. Baek, S. Niu, T. W. Nam, Y. H. Hur, D. Y. Park, G-T. Hwang, M. Byun, Z. L. Wang, Y. S. Jung and K. J. Lee, *Nano Lett.*, 2014, **14**, 7031–7038.
- 23 Z.-H. Lin, G. Cheng, Y. Yang, Y. S. Zhou, S. Lee and Z. L. Wang, *Adv. Funct. Mater.*, 2014, **24**, 2810–2816.
- 24 W. Seung, H.-J. Yoon, T. Y. Kim, H. Ryu, J. Kim, J.-H. Lee, J. H. Lee, S. Kim, Y. K. Park, Y. J. Park and S.-W. Kim, *Adv. Energy Mater.*, 2016, **6**, 1600988.
- 25 K. Y. Lee, J. Chun, J.-H. Lee, K. N. Kim, N.-R. Kang, J.-Y. Kim, M. H. Kim, K.-S. Shin, M. K. Gupta, J. M. Baik and S.-W. Kim, *Adv. Mater.*, 2014, **26**, 5037–5042.
- 26 J. Chun, J. W. Kim, W.-S. Jung, C.-Y. Kang, S.-W. Kim, Z. L. Wang and J. M. Baik, *Energy Environ. Sci.*, 2015, **8**, 3006–3012.

CHAPTER 4. PVDF GRAGTED PtBA COPOLYMERS

4.1 Introduction

Dielectric materials, commonly referred to as electrical insulators, have received much attention owing to their strong electron bonding, good support of electric fields, and low energy loss.¹⁻³ Polarization and depolarization that occur in dielectrics as a result of an external electric field has been investigated to efficiently charge and discharge electricity, which are very useful when applied to capacitors.⁴⁻⁶ Dielectrics have also been widely used in many applications such as transistors,^{7,8} photovoltaic devices,^{9,10} and electrical insulation.¹¹

Recently, triboelectric nanogenerator (TENG), which converts mechanical energy into electricity, has been suggested as a new energy harvesting technology. Since 2012, it has been proven as a cost effective, simple, and efficient technique for the realization of various self-powered systems, such as sensors,^{12,13} charging systems,^{14,15} etc. However, greater output performance is essential for the implementation of TENG in practical applications. Although various strategies to enhance the output performance have been reported, an effective dielectric for creating the device with high performance should be developed because the output power is critically and basically dependent on the density of the charges transferred.^{16,17} So far, various dielectric materials such as polydimethylsiloxane (PDMS),¹⁸ poly(methyl methacrylate) (PMMA),¹⁹ polyimide (PI),²⁰ polyvinylidene fluoride (PVDF),²¹ and polytetrafluoroethylene (PTFE)²² have been used without any modifications and the electrical signals were not enough. Very recently, the modification of properties such as compressibility,¹⁶ surface potential,²³ and hydrophobicity²⁴ in a few TENGs has been reported, however, most of them have focused on partial reports on the effects of the output performance. The parameters mentioned above may be also interrelated to each other. Thereby, the establishment of an interrelated library for the development of dielectrics from materials aspect in TENGs may be needed.

PVDF, a dielectric polymer with a good piezoelectric/pyroelectric response and low acoustic impedance, has been considered as one of the most widely studied dielectric materials in mechanical energy harvesting technologies. In particular, it can be formed in a variety of nanostructures such as nanowire, nanofibers, nanotubes, etc., and can be flexible, therefore, the use of PVDF has been successfully demonstrated in a number of devices, such as capacitors and sensors, as well as TENG.²⁵⁻²⁷

Following the principal that grafting one polymer onto another polymer backbone can combine the benefits of each parent polymer, we set out to design PVDF graft copolymers to

incorporate poly(*tert*-butyl acrylate) (PtBA) through an atom transfer radical polymerization (ATRP) technique, as an efficient dielectric to enhance the output performance of the TENGs. The grafting of PtBA onto the PVDF backbone suppressed the formation of the β phases; hence, the PVDF-Gn graft copolymers were mainly composed of the α phases. As the grafting ratio increased to 18 %, the dielectric constant values increased from 8.6 to 16.5 in the frequency range of $10^2 - 10^5$ Hz, which were attributed to the increase of the net dipole moment of the materials, supported by the Kelvin probe force microscopy measurements (KPFM). The TENG fabricated with the graft copolymer generated the output voltage and current density of 64.4 V and $18.9 \mu\text{A}/\text{cm}^2$, twice the enhancement in both, compared to pristine PVDF based TENG. Further increase in the output performance to 105 V and $25 \mu\text{A}/\text{cm}^2$, 20 times enhancement in output power, was also obtained by tuning the surface potential via poling method, which improved the charges accepting characteristics. The enhanced output performance was quite stable and reliable under harsh mechanical environment due to the high flexibility of the film. A much faster charging property was also demonstrated in this study.

4.2 Experimental details

4.2.1 Materials and Instruments

PVDF (KF1100, $M_n = 168.8$ kDa, PDI = 2.94) was purchased from Kureha. *tert*-Butyl acrylate (tBA) was purchased from Sigma-Aldrich and was passed through an aluminum oxide column to remove the inhibitor before use. Copper (I) chloride (CuCl , 99.999%) and 1,1,4,7,10,10-hexamethyltriethylenetetramine (HMTETA) were purchased from Alfa Aesar Chemical Company. 1-Methyl-2-pyrrolidone (NMP) was purchased from JUNSEI. All solvents were reagent grade, and all reagents were used as received. The molecular weights of PVDF and the graft copolymers were measured by gel permeation chromatography (GPC) conducted at 23°C in DMF at a flow rate of 1 mL/min, using a Agilent 1260 Infinity GPC system equipped with a PL gel $5 \mu\text{m}$ mixed B column (Polymer Laboratories) and differential refractive index detectors. Monodisperse PS standard (Polymer Laboratories) was used for calibration. ^1H NMR was performed in deuterated DMF, using a 400-MR DD2 (Agilent, USA) 400 MHz spectrometer. The Fourier transform infrared (FT-IR) spectra were recorded on a 670-IR (Agilent, USA) spectrophotometer.

4.2.2 Synthesis of PVDF-Gn graft copolymers

PVDF-Gn graft copolymers were helped with synthesis and characterization in the Prof. Yang's laboratory. PVDF (3.0 g) was dissolved in NMP (30 ml) at 60°C. Once the PVDF had completely dissolved in NMP, *tert*-butyl acrylate (18.02 g, 93.5 mmol), CuCl (0.03 g, 0.202 mmol), and HMTETA (0.127 g, 0.367 mmol) were added to the PVDF solution at room temperature under an argon atmosphere. Then, the reaction mixture was heated at 120°C for a certain reaction time (either 12, 24 or 72 h). After cooling to room temperature, the copolymer solution was poured into water–methanol (1:4 v/v) and filtered off. The precipitated copolymer was stirred overnight in a large volume of hexane. Then, the copolymer was recovered by filtration, re-dissolved in NMP, and precipitated into the water: methanol (1:4 v/v). Finally, the graft copolymers were dried under a vacuum. ¹H NMR (400 MHz, C₃D₇NO): δ (ppm) 2.9 – 3.2 (br, 2H, -CF₂-CH₂-CF₂-CH₂-), 2.3 – 2.5 (br, 2H, -CF₂-CH₂-CH₂-CF₂-), 1.4 – 1.65 (br, 9H, -C(CH₃)₃). PVDF-G10: $M_n = 180.0$ kDa, PDI = 1.58, PVDF-G15: $M_n = 201.8$ kDa, PDI = 1.56, PVDF-G18: $M_n = 218.5$ kDa, PDI = 1.47.

4.2.3 Production of PVDF-based triboelectric nanogenerator

In the experiment, first, the synthesized PVDF-Gn solution was cast into a film shape in a blocking layer on SiO₂/Si substrate and dried in the atmosphere at 60°C for 10 min to remove the DMF solution. This layer was then maintained at 90°C for 5 h and then cooled at room temperature. After The PVDF-Gn film layer was peeled off from the substrate, the PVDF-Gn film of 30 μm was obtained. To fabricate the TENG, a Kapton film was glued between Al foil and PVDF-Gn film, followed by the attachment of Al electrode on the opposite side of Kapton film, which acts as the top layer. The spacer between the bottom electrode and the PVDF-Gn film was made of four springs with a length of 5 mm in each corner. Finally, PVDF-Gn based TENGs were obtained. The effective area and gap distance of both PVDF and PVDF-Gn films were 2 cm × 2 cm and 1 mm, respectively.

4.2.4 Characterization and measurements

The morphologies of PVDF-based films were further characterized by a field emission-scanning electron microscope (FE-SEM). The dielectric constants of the PVDF-based films

were measured by an impedance analyzer (Agilent) over the frequency range of 10^2 Hz to 10^6 Hz at room temperature. A pushing tester (Labworks Inc., model no. ET-126-4) was used to create vertical compressive strain in the TENG. A Tektronix DPO 3052 Digital Phosphor Oscilloscope and a low-noise current preamplifier (model no. SR570, Stanford Research Systems, Inc.) were used for electrical measurements. Nanoindentation tests were carried out at a constant indentation strain rate of 0.05 s^{-1} , with a maximum indentation depth of $20 \text{ }\mu\text{m}$, with Berkovich indenter, using the DCM II module in Nanoindenter G200 made by Agilent Corporation. The KPFM measurements were carried out using Park systems XE-100 with Pt/Cr-coated silicon tips (tip radius $< 25 \text{ nm}$, force constant 3 Nm^{-1} , and resonance frequency of 75 kHz). $3 \text{ }\mu\text{m} \times 3 \text{ }\mu\text{m}$ size KPFM images were scanned at a scanning speed of 0.5 Hz in the noncontact mode with a 2 V_{ac} signal with a frequency of 17 kHz . Ultraviolet photoelectron spectroscopy (UPS) (Thermo Fisher, ESCALAB 250Xi) was performed using the He I ($h\nu = 21.2 \text{ eV}$) photon line of a He discharge lamp under ultra-high vacuum conditions for the measurement of the work function.

4.3 Results and Discussion

4.3.1 Synthesis of PVDF-Gn graft copolymers

The PtBA-grafted PVDF copolymers were prepared by using ATRP (Figure 5a), in accordance with previously established methods in the literature.²⁸ PVDF-Gn graft copolymers were helped with synthesis and characterization in the Prof. Yang's laboratory. The grafting ratios were controlled as a function of various reaction times ($12 - 72 \text{ h}$) under the same conditions, yielding three samples with a different number of average molecular weights ($M_n = 180.0 - 218.5 \text{ kDa}$). In a careful inspection of ^1H NMR spectra of the samples (Figure 5b), the composition of the graft copolymers was calculated on a mole basis from the integral ratio of the two noticeable resonances at $2.3 - 2.5$ and $2.9 - 3.2$ ppm attributed to head-to-tail and head-to-head configurations of PVDF and the signals at $1.4 - 1.65$ ppm associated with the *tert*-butyl group in PtBA, by using the following equations;²⁹

$$x = \frac{(\text{Integral}_{1.4-1.65}) / 9}{(\text{Integral}_{2.3-2.5} + \text{Integral}_{2.9-3.2}) / 2} \quad (6)$$

$$\text{PtBA mole percent (mol\%)} = \frac{x}{1+x} \times 100 \quad (7)$$

The mole percent of PtBA in the graft copolymer was determined as 10, 15 and 18%, respectively. The graft copolymers were designated PVDF-Gn in this study, where Gn refers to the mole percent of PtBA grafting. In addition, as shown in Figure 5c, the FT-IR spectra of the PVDF-Gn showed the appearance of the absorption bands at 1725 cm^{-1} assigned to the stretching vibrations of the ester carbonyl groups, in contrast with pristine PVDF. Also, as the grafting ratios of PtBA were increased, the gradually enhanced intensity of the carbonyl bands relative to the methylene stretching bands of PVDF at about 1404 cm^{-1} was observed, which further substantiates the PtBA content determined above.

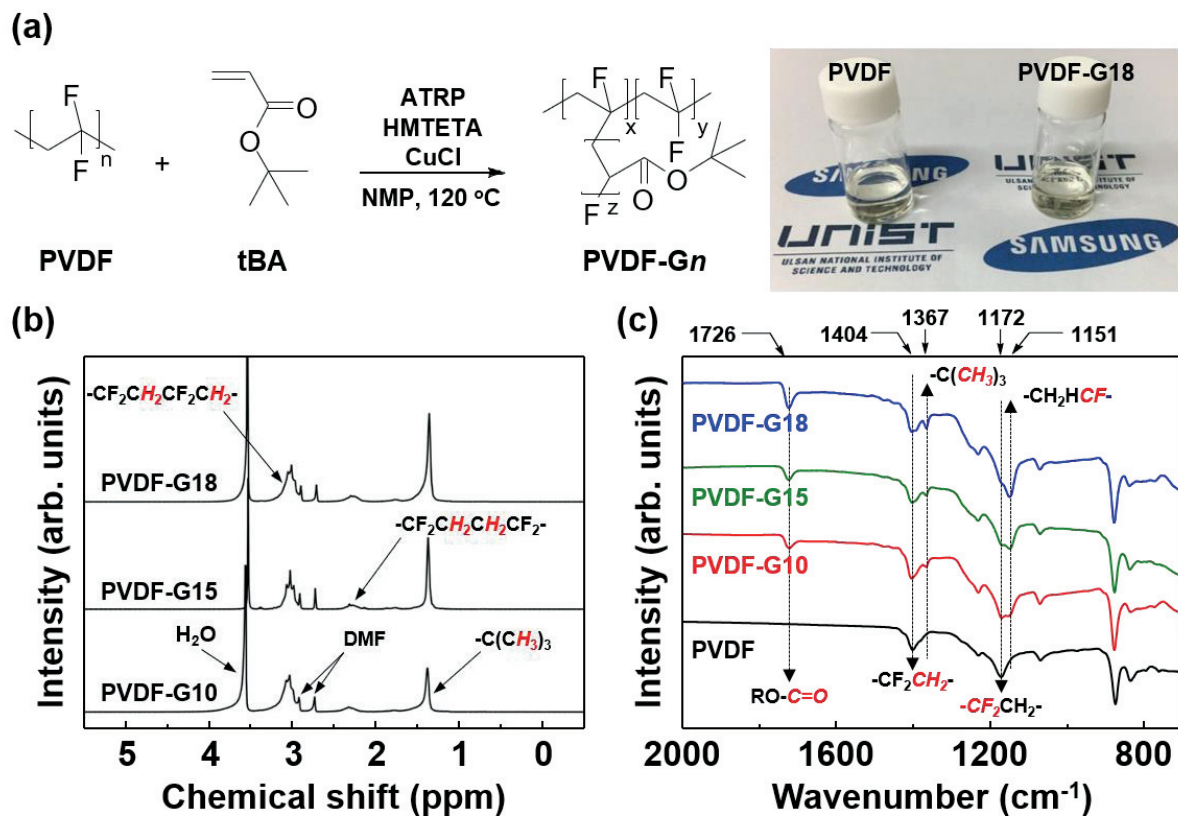


Figure 5. (a) Synthesis of PVDF-Gn graft copolymers and photograph of the PVDF and PVDF-G18 NMP solutions, respectively. (b) $^1\text{H NMR}$, (c) FT-IR of PVDF and PVDF-Gn.

4.3.2 Fabrication of PVDF-Gn based TENGs and its output performance

As for a dielectric, the solutions were casted on the very flat Si/SiO₂ substrate with the blocking layer. After annealing process, the film was peeled off from the substrate and glued on Al film by using the Kapton film, followed by the attachment of Al electrode to fabricate the TENG, as shown in Figure 6a and 6b. The detailed experimental procedures are also

described in experimental section. Figure 6b also shows that the resultant film appears white and quite flexible after peeled off. The TENG has $2\text{ cm} \times 2\text{ cm}$ of active area with the spacer between the bottom electrode and the PVDF-Gn film made of four springs in each corner. The output voltages and current densities of the TENGs were measured and plotted in Figure 6c and Figure 7. Cycled compressive force of around 50 N at an applied frequency of 10 Hz was applied. The TENG with pristine PVDF film shows small AC-type electrical output performance of less than approximately 32.9 V and $7.7\ \mu\text{A}/\text{cm}^2$. For the PVDF-G10, the output voltage and current density were increased to 45 V and $8.3\ \mu\text{A}/\text{cm}^2$, respectively. Furthermore, the highest enhancement (with an output voltage of 64.4 V and current density of $18.9\ \mu\text{A}/\text{cm}^2$) was observed in PVDF-G18 under the same mechanical force. To show the high output performance of the TENG, various polymers such as polyimide, polytetrafluoroethylene, and polyvinyl chloride were used as dielectrics in the TENGs and the electrical output performances were measured. Figure 8 shows that the TENG with PVDF-G18 film generated the largest output voltage and current density, compared with those with other polymers. The instantaneous power densities were also obtained by measuring the output voltages and current densities of the PVDF-G18-based TENG with external loads from $1\ \Omega$ to $1\ \text{G}\Omega$, plotted in Figure 6c. At $10\ \text{M}\Omega$, approximately $0.45\ \mu\text{A}/\text{cm}^2$ was obtained, a 20 times enhancement compared with pristine PVDF-based TENG in Figure 9.

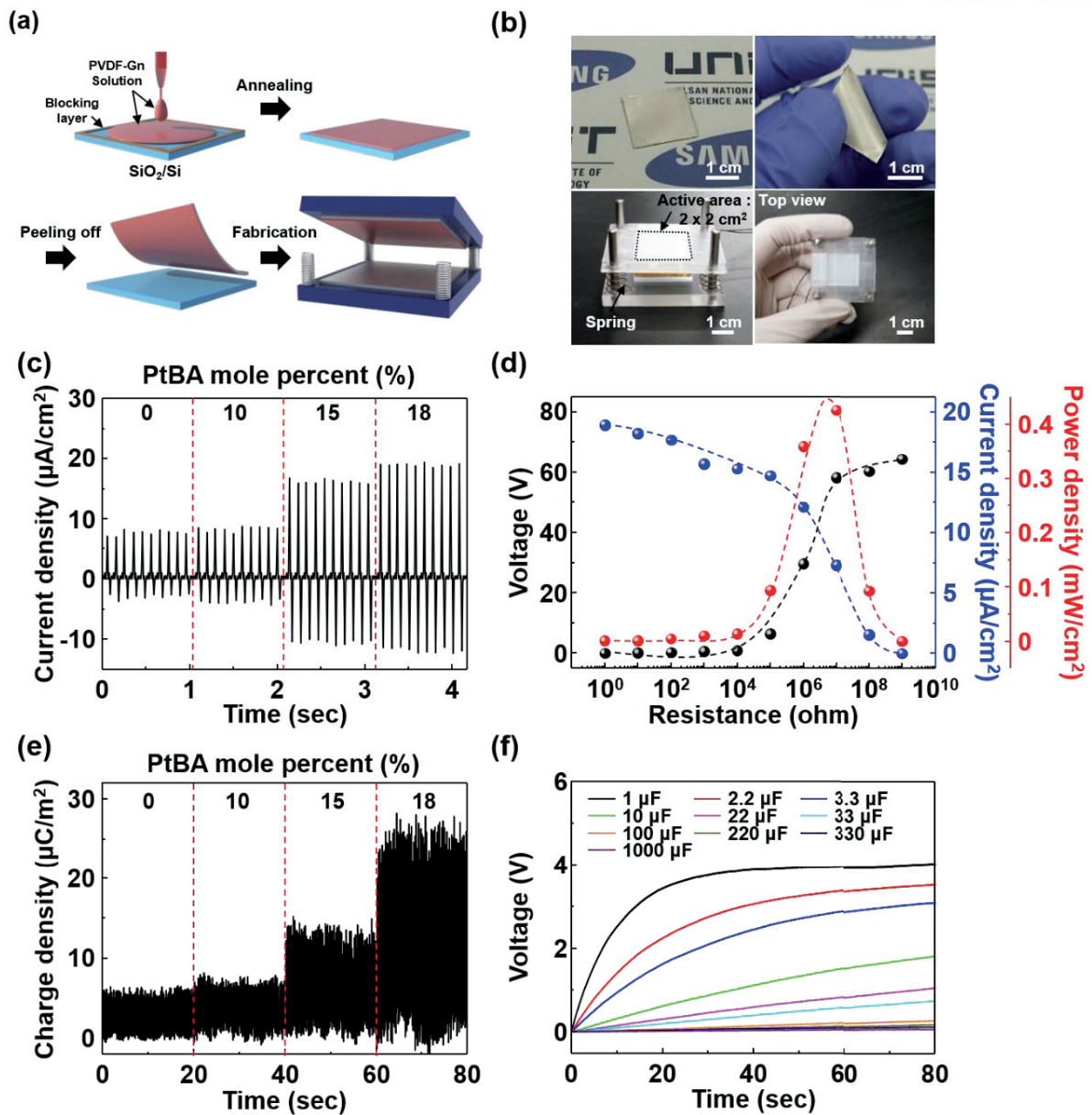


Figure 6. (a) Schematic diagrams of the fabrication process for the PVDF-Gn based TENGs. (b) Photographs of a flexible PVDF-Gn film after peeled off and a PVDF-Gn based TENG. (c) The output current densities generated by the PVDF-based TENGs as a function of the PtBA mole percent ranging from 0 to 18%. (d) The output voltages, current densities, and the output power densities of the PVDF-G18 based TENG with the resistance of external loads from 1 to $10^9 \Omega$. (e) Charge densities generated by the PVDF-based TENGs as a function of the PtBA mole percent ranging from 0 to 18%. (f) The measured voltage of a commercial capacitor (1, 2.2, 3.3, 10, 22, 33, 100, 220, 330, 1000 μF) charged with AC to DC signal converting circuit by using PVDF-G18 based TENG.

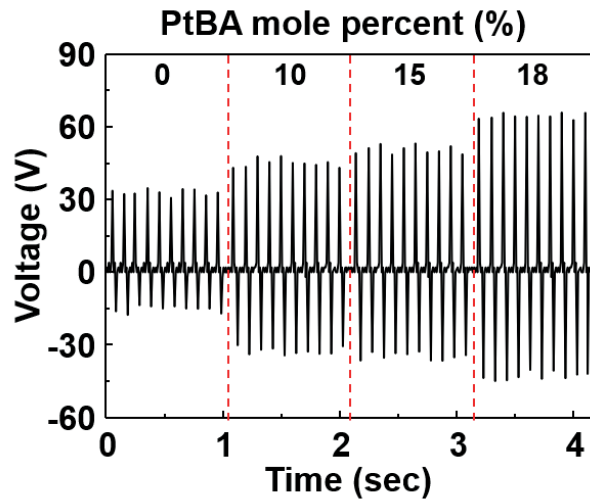


Figure 7. The output voltages generated by the PVDF-based TENGs as a function of the PtBA mole percent ranging from 0 to 18%.

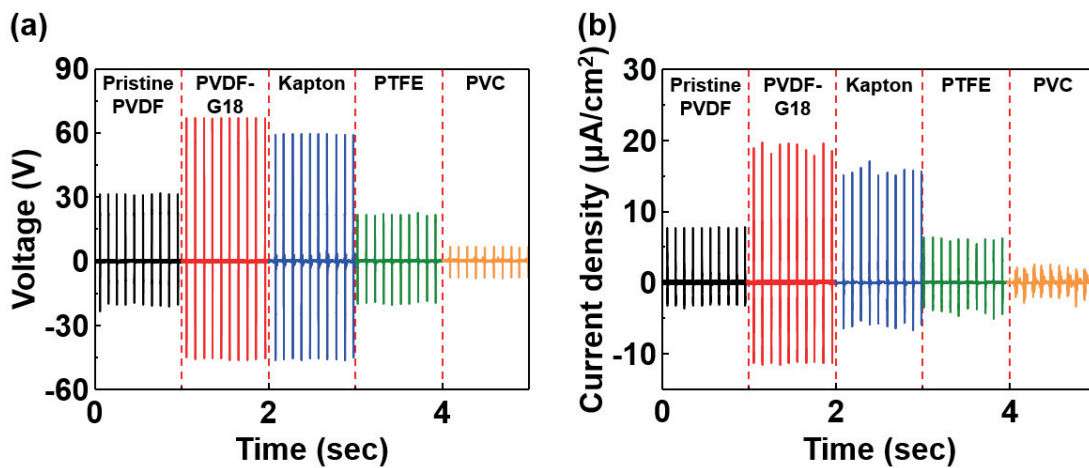


Figure 8. (a) The output voltages generated by the different polymer based TENGs. (b) The output current densities generated by the different polymer based TENGs.

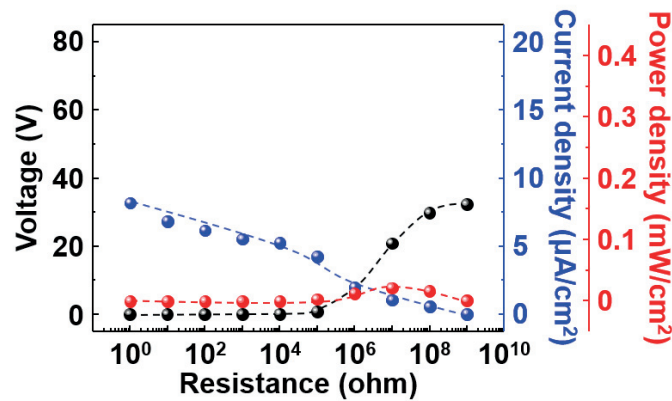


Figure 9. (a) The output voltages generated by the different polymer based TENGs. (b) The output current densities generated by the different polymer based TENGs.

The transferred charge density of all samples significantly increased with the mole percent, showing good agreement with the simulation and experimental results in Figure 6d, 10, and 11. According to previous reports,¹⁶ it is obvious that the dielectric constant of the dielectric plays a very important role in determining the electrical output performance of the TENG. The total transferred charge density (σ') on the top electrode of the TENG can be expressed as;³⁰

$$\sigma' = \frac{-\sigma_0 d_{gap}}{d_{gap} + d_{PVDF} / \epsilon_{PVDF}} \quad (8)$$

where σ_0 is the triboelectric charge density at the equilibrium state, d_{gap} and d_{PVDF} are the gap distance and the thickness of PVDF-based films, and ϵ_{PVDF} is a dielectric constant of PVDF-based films. According to equation (8), the obtained σ' can increase as the dielectric constant increases. By using the COMSOL multi-physics software, we also calculated electrostatic potentials inside the TENG with PtBA mole percent, as shown in Figure 11. When the TENG is fully released if we assume the electric potential (U_{bottom}) of the surfaces of the bottom layer to be zero, the electric potential of the surfaces of the top dielectric layer (U_{top}) can be expressed by $U_{top} = \sigma' d_{gap} / \epsilon_0$, where σ' is the total transferred charge density, ϵ_0 is the vacuum permittivity of free space (8.854×10^{-12} F/m), and the gap distance (d_{gap}) of the TENG can be calculated as $d_{gap} = 1$ mm. Dielectric constant of PVDF-Gn film could be obtained from results in 9.1 to 16.5. It is clear that the potential increases with PtBA mole percent, meaning that the output power of the TENG will be enhanced.

To show the practical application, we evaluated the capacitor charging characteristic of the TENGs, which were integrated with AC to DC converting circuit in Figure 12a. The converting circuit consists of one rectifier, three low capacitors ($3 \times 0.001 \mu\text{F}$) and one capacitor (1, 2.2, 3.3, 10, 22, 33, 100, 220, 330, 1000 μF) to convert AC to DC output signal. When the vertical compressive force of 50 N under frequency of 10 Hz was applied, the capacitors were charged up to approximately 4 V when a 1000 μF capacitor was used. It was also clearly seen that the capacitor charge by the PVDF-G18 based TENG was much faster and the voltage charged was larger by twice, compared with pristine PVDF based TENG (Figure 12b).

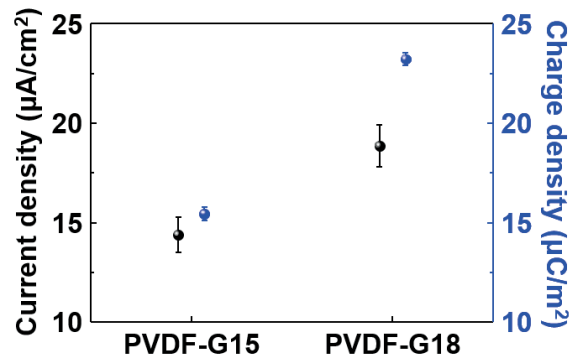


Figure 10. Average current density and charge density generated by the PVDF-G15 and -G18 based TENG. Error bars represent standard error of the mean (S.E.M.).

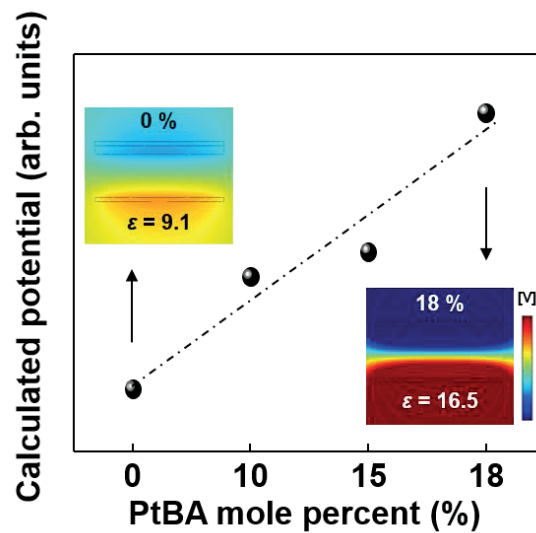


Figure 11. The calculated electrostatic potentials inside the nanogenerator with PtBA mole percents ranging from 0 to 18%.

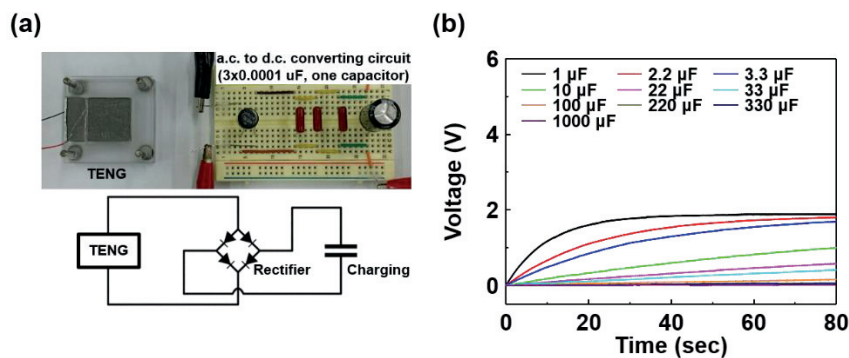


Figure 12. (a) Optical images of the portable power-supplying system with AC to DC converting circuit and (b) The measured voltage of a commercial capacitor (1, 2.2, 3.3, 10, 22, 33, 100, 220, 330, 1000 µF) charged with AC to DC signal converting circuit by using pristine PVDF based TENG.

4.3.3 Mechanical stability and durability of PVDF-Gn based TENG

Figure 13 shows the flexibility and durability of the PVDF films based TENG. To show the flexibility, the films were bended 3000 times, as shown in Figure 13a, and the output current densities were measured, compared with those measured before the bending. As shown in Figure 13b, the both TENGs do not show significant change in the output current densities before and after bending, indicating that the films are quite stable under the harsh environment. The PVDF-G18 based TENG still generated higher output current than the pristine PVDF based one. The output current density generated by the PVDF-G18 based TENG does not also appear to change significantly at 18,000 cycles during the test. These result reveals the robustness and mechanical durability for a practical TENG (Figure 13c).

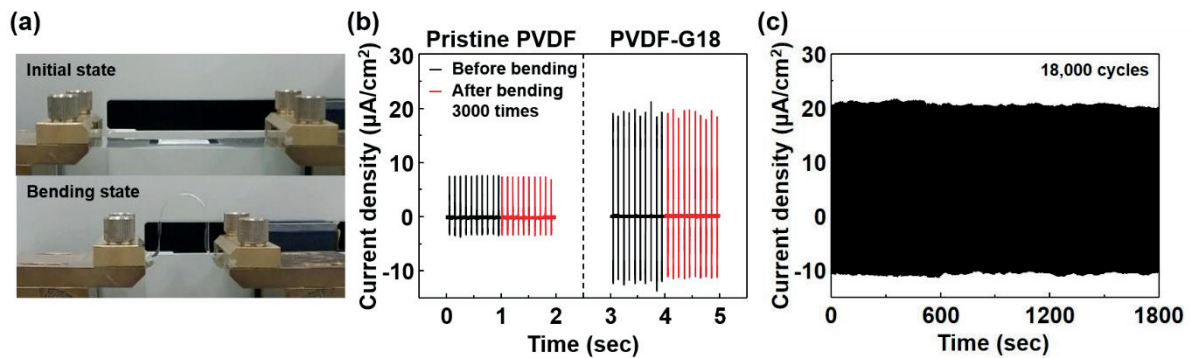


Figure 13. (a) Mechanical bending tests of the PVDF-based TENG. (b) The output current densities generated by the pristine PVDF-based and the PVDF-G18 based TENGs before and after bending 3,000 times. (c) Stability and durability test of the TENG under cycled compressive force of 50 N over 18,000 cycles.

4.3.4 AFM, SEM, and Nanoindentation test for the PVDF-Gn films

The enhancement in output power by the grafting was analyzed in many ways because there are many factors influencing the output power such as the surface roughness of the contact layers, the compressibility of the triboelectric materials, the dielectric properties, the surface potentials, etc.^{16,17,23,31} Furthermore, the factors may be interrelated to each other, meaning that a main reason was not easy to be found. First, we evaluated the surface morphology of the PVDF-Gn films measured by using atomic force microscopy (AFM), as shown in Figure 14a. The root-mean-square (RMS) roughness value was measured to be approximately 98.11 nm at the PVDF-G18 and there is no significant change as the mole percent decreases from 18 to 0 %,

as shown in Figure 14a. Actually, we strived to minimize the effect of the roughness by casting the solution on the very flat Si/SiO₂ substrate and peeling off the film to make a very flat PVDF surface because an important factor in enhancing the output performance of the TENG is to increase the surface roughness. These results may imply that the effect of the roughness on the output power is negligible.

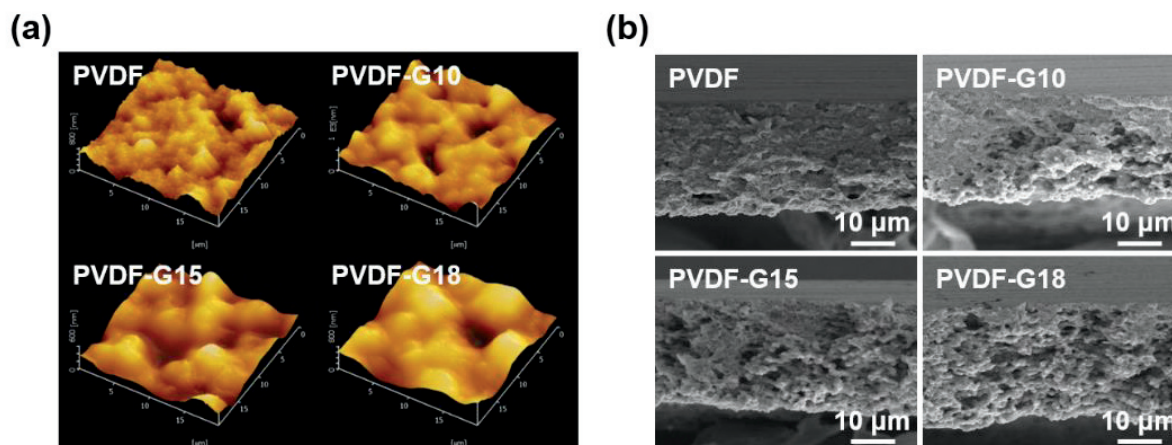


Figure 14. (a) 3-dimensional AFM images and (b) Cross-sectional SEM images for PVDF-based films with various PtBA mole percent ranging from 0 to 18%.

The cross-sectional scanning electron microscope (SEM) images of the PVDF-G_n films with the grafting ratio were shown in Figure 14b. Here, the thickness of all the films was fixed to approximately 30 μm. Importantly, all the films were quite porous, which is most likely due to the slow solvent removal process at low temperature (~ 60°C) to remove solvents. Such porous structures have been proven to be so effective in enhancing the output power because the output performance was significantly dependent on compressibility.¹⁶ Here, to measure the compressibility of the films, we evaluated resistance to deformation by external force by using the Berkovich indenter which induces much higher local strain than uniaxial compression. The loading and unloading curves measured by a nanoindentation test on the PVDF-based films were shown in Figure 15. The nanoindentation results show that plastic collapse occurs in all samples during loading and unloading. The loading-unloading curves for PVDF-based films in Figure 15a indicate their repeatable plastic deformation, with the same displacement depth of approximately 1 μm when in uniaxial compression. Based on the nanoindentation test (Figure 15b), one can conclude that there is no change in the elastic modulus and hardness of PVDF-based films, meaning that the films exist partially elastic recovery which are not perfectly elastic recovery and are mixed with the elastic-plastic transition.

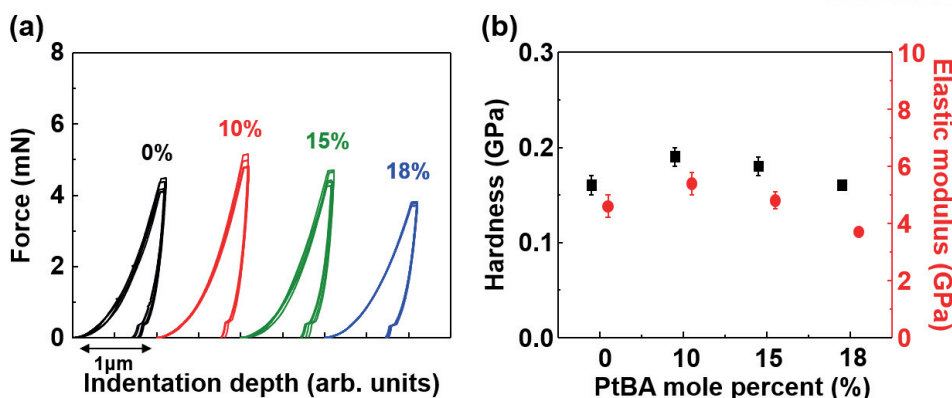


Figure 15. (a) The loading and unloading curves measured by nanoindentation test for the PVDF-Gn film of the mole percents (0, 10, 15, and 18%) of PtBA. (b) The elastic modulus and hardness of PVDF-Gn films of the mole percents (0, 10, 15, and 18%) of PtBA. Error bars represent standard error of the mean (S.E.M.).

4.3.5 Dielectric properties for PVDF-Gn films

With two important factors excluded, we measured the frequency dependent dielectric properties of the PVDF-based films over the frequency range of 10^2 Hz to 10^6 Hz at room temperature, plotted in Figure 16. To measure the dielectric constants, PVDF-based films were prepared on an Au/Si substrate, and Au as a top electrode was then deposited by using an E-beam evaporator. For pristine PVDF film, the dielectric constant was measured to be approximately 8.6 in the frequency range of $10^2 - 10^5$ Hz; almost the same as in previous reports.^{32,33} There is a significant drop in dielectric constant in the higher frequency range ($10^5 - 10^6$ Hz). This is because the dipole relaxation of the polymers cannot catch up with the external oscillating field. As the grafting ratios in the backbone increased, the dielectric constant gradually increased. Consequentially, the PVDF-G18 shows a superior dielectric constant value of up to 16.5 (Figure 17). There is no significant change in the loss tangent (~ 0.03) of all samples, except those in the higher frequency range. This means that the dielectric constant values are quite reliable. In principle, the dielectric constant has a strong correlation with polarizability and free volume of the elements present in the materials, as formulated in the Clausius-Mossotti equation.³⁴ The π -bonding and polar characteristics of the ester groups ($-\text{COO}-$) in the PtBA are able to not only hold relatively great polarizability, but also increase the net dipole moment in the backbone, which are considered to be major factors contributing to the improvement of dielectric constant values in the graft copolymers.³⁴

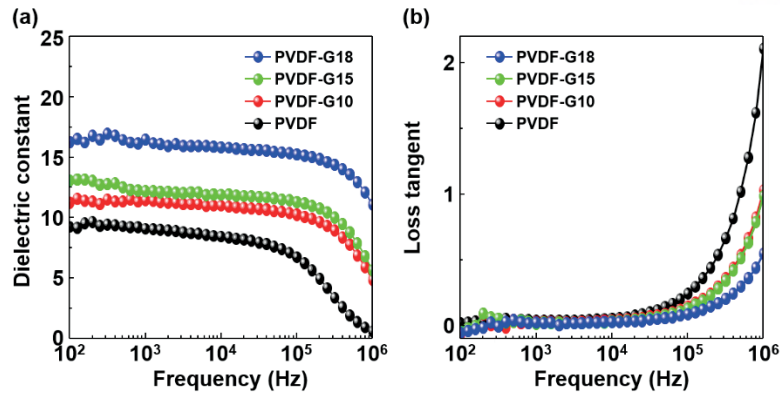


Figure 16. Frequency dependence of (a) dielectric constant values and (b) loss tangent for PVDF-based films with various PtBA mole percent ranging from 0 to 18%.

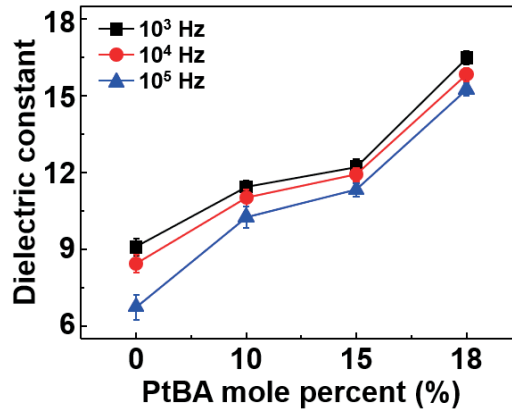


Figure 17. The dielectric constant of PVDF-Gn films according to the mole percent (0, 10, 15, and 18%) of PtBA. Error bars represent standard error of the mean (S.E.M.).

4.3.6 Relationship between the dielectric constant and output performance

To investigate more clearly the relationship between the dielectric constant and output performance of the TENG, we compared the output currents of PVDF-based TENGs as a function of measuring time, as plotted in Figure 18a. The output current increases with the mole percent. It is worth mentioning that the time taken for the output to reach 90 % of the final current also increases with the mole percent from 3.15 (\pm 0.51) s to 14.48 (\pm 0.58) s, as plotted in Figure 18b. In general, in a film-type capacitor, the accumulated charges (Q) can be expressed as;

$$Q = CV \left[1 - e^{-\frac{t}{RC}} \right] \quad (9)$$

where C , V , t , and R are capacitance, input voltage, charging time, and resistance, respectively. Assuming that V is constant, C can be calculated using equation $C = \epsilon_0 \epsilon_r A / d$, where ϵ_0 , ϵ_r , A , and d are the permittivity of free space ($8.854 \times 10^{-12} \text{ Fm}^{-1}$), dielectric constant of material, contact area (4 cm^2), and distance ($30 \text{ }\mu\text{m}$) between top and bottom electrodes, respectively. Thus, the charges can be expressed with the dielectric constant in Figure 18c. As the dielectric constant increases by two times, the charges increase by two times and the saturation time also increases from 2.3 to 4.52 s; a good agreement with the experimental results. This indicates that the increase in the dielectric constant can enhance the maximum charge density that can be sustained on the surface of the dielectric.

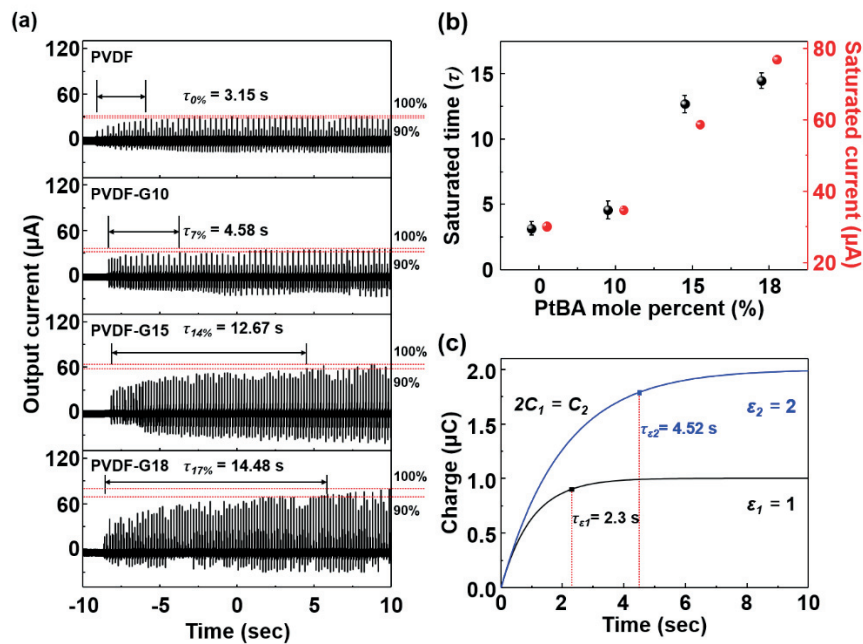


Figure 18. (a) Measured output currents of the PVDF-based TENG with the grafting ratio. (b) Saturated time and output current as a function of the PtBA mole percent ranging from 0 to 18%. Error bars represent standard error of the mean (S.E.M.). (c) Calculated charging time of the capacitor increases from 2.3 sec to 4.52 sec with the increase of the dielectric constant.

4.3.7 Surface potential and UPS measurement of PVDF-Gn films

Finally, we further measured the surface potential difference of the pristine PVDF and PVDF-G18 to understand an important parameter that can affect output performance (Figure 19a) by the KPFM tools, compared to the Pt coated Si tip. The surface potential values were calculated as -156 mV for Au film and -370 mV for PVDF film, while PVDF-G18 showed a relatively higher potential value of +260 mV. If the surface potential of Al is not changed during the full cycle, the measured surface potential values indicate that the difference in work

function between Al and PVDF-G18 is smaller than that between Al and pristine PVDF, as shown in Figure 19b. The decrease in work function with the grafting was supported by ultraviolet photoelectron spectroscopy (UPS) spectra, as shown in Figure 19c. The work function can be determined from the difference between the incident light energy ($h\nu = 21.22$ eV) and the energy of the secondary cutoff (E_{cutoff}) as $W = h\nu - (E_{cutoff} - E_F)$. The onset of secondary electron peak shifted toward lower binding energy by 1.19 eV for pristine PVDF and 0.48 eV for PVDF-G18, compared with Al. Based on these results, the work function can be estimated to be approximately $5.55 (\pm 0.19)$ eV and $4.84 (\pm 0.16)$ eV in pristine PVDF and PVDF-G18, respectively (Figure 19d), which is a good agreement with the KPFM results. According to previous papers, it is expected that the electron transfer from the Al to PVDF-G18 is not effective, therefore, the output performance of the TENG should be decreased because of the low electric potential generated between them.

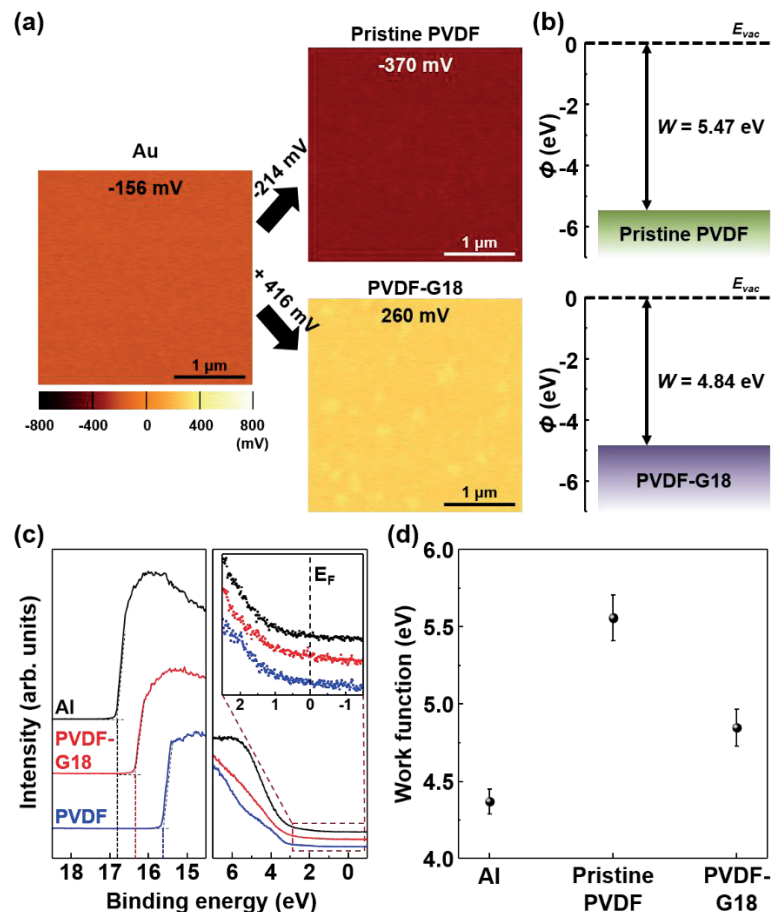


Figure 19. (a) KPFM surface potential distribution images ($3 \mu\text{m} \times 3 \mu\text{m}$) of Au, pristine PVDF, and PVDF-G18 films. (b) The work function values of pristine PVDF and PVDF-G18 films, obtained from the KPFM results. (c) UPS spectra and (d) the change in work function of Al, pristine PVDF, and PVDF-G18 film. Error bars represent standard error of the mean (S.E.M.).

4.3.8 XRD pattern of PVDF-Gn films

The decrease of the work function in PVDF-G18 may be explained in terms of microstructural change. The crystalline properties of PVDF-based films were characterized by X-ray diffraction (XRD), compared with PVDF film and plotted in Figure 20a. For the PVDF film, two representative peaks at 17.9° and 20.6° were observed. We thought that the two peaks would correspond to the (100) plane of α phase and the (200) plane of β phase, respectively. However, it was found that the β (200) peak, which was quite asymmetric, could be deconvoluted into two peaks, α (110) and β (200),³⁵ as shown in Figure 20b. With the grafting, the peak intensity of α (110) significantly increased, while the β (200) peak almost disappeared. In general, β phase is known to be formed due to the rotation of the CF_2 chains when annealed.³⁶ The chain mobility is strongly related to the structure of the molecules, molecular weight, chain length, etc.³⁷ This implies that the increase in the molecular weight and the steric bulkiness can suppress the rotation of the chains in PVDF-Gn films, thereby, β phase is not likely to be formed.

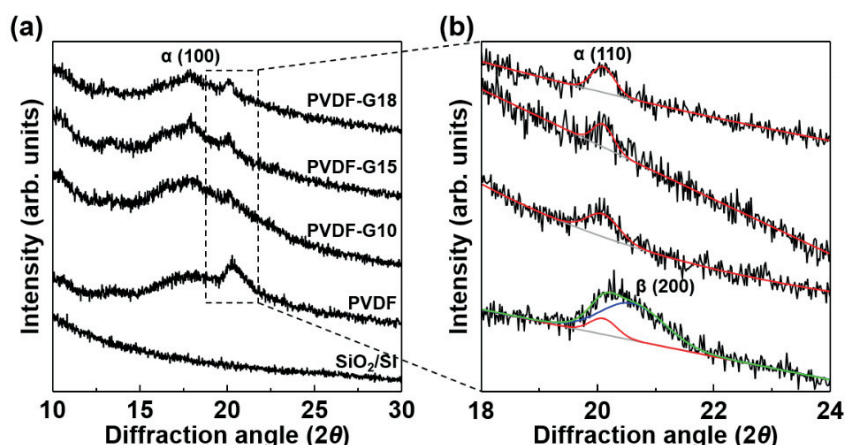


Figure 20. (a) The high-resolution XRD patterns of pristine PVDF and PVDF-Gn films as a function of PtBA mole percent. (b) The expanded view of the 2nd peak in Figure 20a. The peak can be deconvoluted into two peaks, α (110) (red) and β (200) phase (blue).

4.3.9 Output performance depending on the poling electric field direction

In general, the dipole moment originates from the asymmetric structure of the β phase in PVDF film and is known to be directed toward the surface of the film. This is because CF_2 dipoles are rotated by the thermal energy and dipole moments that are uniformly aligned in parallel to the substrate.^{38,39} However, the β phases significantly decreased in PVDF-Gn films.

The increase in net dipole moments, thus, may be attributed to the formation of the polar molecules, that is, polar β phase. In general, the change in the surface potential (ΔV) is defined through the Helmholtz equation;³⁴

$$\Delta V = 4\pi \frac{NP_0 \cos(\theta)}{A\varepsilon} \quad (10)$$

where A is the surface area, N is the number of molecules, P is the dipole moment, P_0 is the dipole moment of the free molecule in a vacuum, θ is the molecular tilt angle, and $\varepsilon = (P_0/P)$ is the effective dielectric constant of a molecular monolayer. The surface potential changes of $\Delta V = -214$ mV for pristine PVDF and $\Delta V = +416$ mV for PVDF-G18 result in the dipole moments of 1.26 D and 3.41 D with opposite direction, respectively. By the KPFM result, the net dipole moment in PVDF-Gn films is believed to be directed toward the substrate, opposite to that in the β phase, as shown in Figure 21. In general, the direction is influenced by the chain structure.³⁴ In the β phase in PVDF film, high dipole moment of $-\text{CF}_2$ units is aligned on the same side. Whereas as the grafting ratio increased, the extent of dipole orientation for the C–F bonds directing parallel to each other decreased, resulted in the opposite net dipole direction of the PVDF-Gn film.³⁴ Thus, one can conclude that the increase in the dielectric constant value is a dominant factor in enhancement in the output power of the TENG.

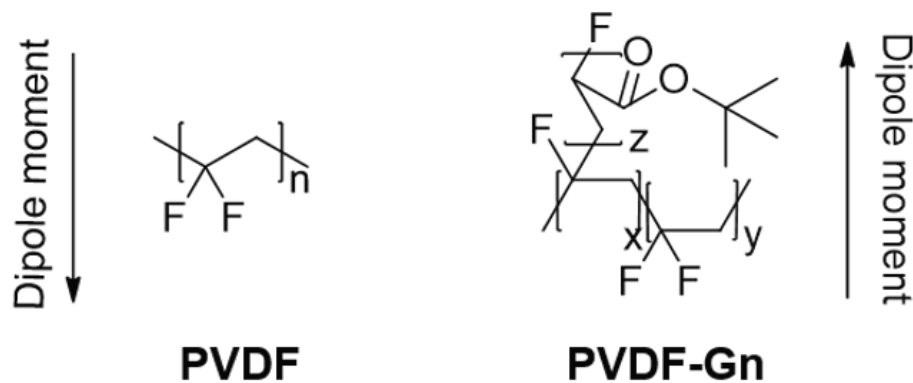


Figure 21. Structures of PVDF and PVDF-Gn.

Based on the measured surface potential of the PVDF film, for further enhancement in the output power, we poled the film at 100 MVm^{-1} for 30 min and aligned the dipole direction to increase the work function difference with the Al. Figure 22 shows the output voltages and the output currents depending on the poling electric field direction. For pristine PVDF film, the TENG generated 65 V and $11 \mu\text{A}/\text{cm}^2$ under forward bias, and -14 V and $-2.7 \mu\text{A}/\text{cm}^2$ under reverse bias. As the grafted 18 %, the output voltage and current density were measured to be

105 V and $25 \mu\text{A}/\text{cm}^2$ under forward bias, and -39 V and $-11 \mu\text{A}/\text{cm}^2$ under reverse bias. The significant increase in the output power of PVDF-Gn is because the positive charges on the surface of forward-polarized PVDF are brought into contact with the aluminum while the other side of its surface is covered by the back electrode.

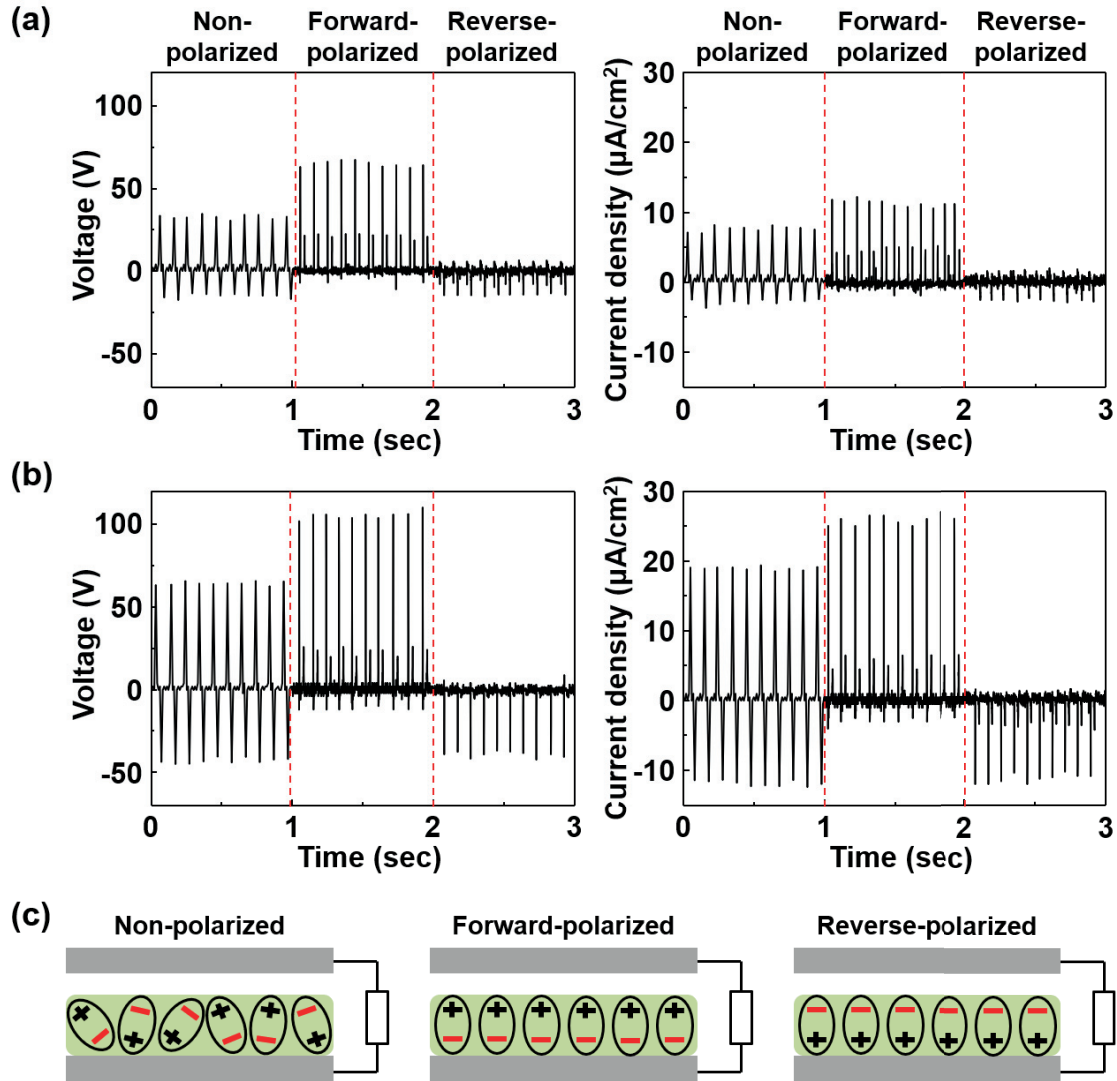


Figure 22. The output voltages and current densities for (a) pristine PVDF and (b) PVDF-G18 based TENGs under different poling electric fields direction. (c) Circuit diagrams and the different performances among TENGs fabricated using different poling electric field direction.

4.4 Conclusion

In summary, we reported a facile approach to enhance the output power of TENG with the successful synthesis of PtBA-grafted PVDF copolymers for dielectric constant control. The copolymers were prepared by using ATRP technique and the PtBA was grafted up to 18 %.

high-resolution XRD spectra, it was found that the β phases significantly decreased; thus, the copolymers were mainly composed of α phases with enhanced dipole moment by π -bonding and polar characteristics of the ester functional groups in the PtBA. As the grafting ratio increased to 18 %, the dielectric constant values increased from 8.6 to 16.5 in the frequency range of $10^2 - 10^5$ Hz, which was attributed to the increase of the net dipole moment, supported by the KPFM measurements. This increase in the dielectric constant increased the density of the charges that can be accumulated on the surface, generating the output signals of 64.4 V and $18.9 \mu\text{A}/\text{cm}^2$, twice the enhancement in both, compared to pristine PVDF based nanogenerator. To prove it, we calculated the accumulated charges on the surface with different dielectric constant values, which showed an excellent agreement with the measured output current values. The enhanced output performance is quite stable and reliable under harsh mechanical environment due to the high flexibility of the films. Further increase in the output signals to 105 V and $25 \mu\text{A}/\text{cm}^2$, 20 times enhancement in output power, was also achieved by poling the film to align the dipole direction, which improved the charges accepting characteristics by increasing the work function of the copolymer. The enhanced output power resulted in much faster charging property.

4.5 References

- 1 W. J. Sarjeant, J. Zirnheld and F.W. MacDougall, *IEEE Trans. Plasma Sci.*, 1998, **26**, 1368–1392.
- 2 Y. Cao, P. C. Irwin and K. Younsi, *IEEE Trans. Dielectr. Electr. Insul.*, 2004, **11**, 797–807.
- 3 S. Ducharme, *ACS Nano*, 2009, **3**, 2447–2450.
- 4 B. Chu, X. Zhou, K. Ren, B. Neese, M. Lin, Q. Wang, F. Bauer and Q. M. Zhang, *Science*, 2006, **313**, 334–336.
- 5 S. Wu, W. Li, M. Lin, Q. Burlingame, Q. Chen, A. Payzant, K. Xiao and Q. M. Zhang, *Adv. Mater.*, 2013, **25**, 1734–1738.
- 6 Q. Chen, Y. Shen, S. Zhang, Q. M. Zhang, *Annu. Rev. Mater. Res.*, 2015, **45**, 433–458.
- 7 M.-H. Yoon, H. Yan, A. Facchetti, T.J. Marks, *J. Am. Chem. Soc.*, 2005, **127**, 10388–10395.
- 8 M. E. Roberts, N. Queraltó, S. C. B. Mannsfeld, B. N. Reinecke, W. Knoll, Z. Bao, *Chem. Mater.*, 2009, **21**, 2292–2299.
- 9 M. T. Dang, L. Hirsch, G. Wantz, P3HT:PCBM, *Adv. Mater.*, 2011, **23**, 3597–3602.
- 10 L. Huo, S. Zhang, X. Guo, F. Xu, Y. Li, J. Hou, *Angew. Chem.*, 2011, **123**, 9871–9876.
- 11 S. Dadbin, M. Frounchi, M. H. Saeid, F. Gangi, *J. Appl. Polym. Sci.*, 2002, **86**, 1959–1969.
- 12 Z. Li, J. Chen, J. Yang, Y. Su, X. Fan, Y. Wu, C. Yu, Z. L. Wang, *Energy Environ. Sci.*, 2015, **8**, 887–896.
- 13 J.-H. Kim, J. Chun, J. W. Kim, W. J. Choi, J. M. Baik, *Adv. Funct. Mater.*, 2015, **25**, 7049–7055.
- 14 S. Wang, L. Lin, Z. L. Wang, *Nano Lett.*, 2012, **12**, 6339–6346.
- 15 Y. Yang, H. Zhang, Y. Liu, Z.-H. Lin, S. Lee, Z. Lin, C. P. Wong, Z. L. Wang, *ACS Nano*, 2013, **7**, 2808–2813.
- 16 J. Chun, J. W. Kim, W.-S. Jung, C.-Y. Kang, S.-W. Kim, Z. L. Wang, J. M. Baik, *Energy Environ. Sci.*, 2015, **8**, 3006–3012.
- 17 J. Chen, H. Guo, X. He, G. Liu, Y. Xi, H. Shi, C. Hu, *ACS Appl. Mater. Interfaces*, 2016, **8**, 736–744.
- 18 G. Zhu, Z.-H. Lin, Q. Jing, P. Bai, C. Pan, Y. Yang, Y. Zhou, Z. L. Wang, *Nano Lett.*, 2013, **13**, 847–853.
- 19 G. Zhu, C. Pan, W. Gu, C.-Y. Chen, Y. Zhou, R. Yu, Z. L. Wang, *Nano Lett.*, 2012, **12**, 4960–4965.

- 20 Z. Zhao, X. Pu, C. Du, L. Li, C. Jiang, W. Hu, Z. L. Wang, *ACS Nano*, 2016, **10**, 1780–1787.
- 21 P. Bai, G. Zhu, Y. S. Zhou, S. Wang, J. Ma, G. Zhang, Z. L. Wang, *Nano Res.*, 2014, **7**, 990–997.
- 22 P. Bai, G. Zhu, Z.-H. Lin, Q. Jing, J. Chen, G. Zhang, J. Ma, Z. L. Wang, *ACS Nano*, 2013, **7**, 3713–3719.
- 23 Y. S. Zhou, S. Wang, Y. Yang, G. Zhu, S. Niu, Z.-H. Lin, Y. Liu, Z. L. Wang, *Nano Lett.*, 2014, **14**, 1567–1572.
- 24 K. Y. Lee, J. Chun, J.-H. Lee, K. N. Kim, N.-R. Kang, J.-Y. Kim, M. H. Kim, K.-S. Shin, M. K. Gupta, J. M. Baik, S.-W. Kim, *Adv. Mater.*, 2014, **26**, 5037–5042.
- 25 A. V. Shirinov, W. K. Schomburg, *Sens. Actuat. A*, 2008, **142**, 48–55.
- 26 Y. Song, Y. Shen, H. Liu, Y. Lin, M. Li, C.-W. Nan, *J. Mater. Chem.*, 2012, **22**, 8063–8068.
- 27 M. Li, H. J. Wondergem, M.-J. Spijkman, K. Asadi, I. Katsouras, P. W. M. Blom, D. M. de Leeuw, *Nat. Mater.*, 2013, **12**, 433–439.
- 28 E. Fernández, C. Mijangos, J.-M. Guenet, M. T. Cuberes, D. López, *Eur. Polym. J.*, 2009, **45**, 932–939.
- 29 F. Guan, L. Yang, J. Wang, B. Guan, K. Han, Q. Wang, L. Zhu, *Adv. Funct. Mater.*, 2011, **21**, 3176–3188.
- 30 Z.-H. Lin, G. Cheng, Y. Yang, Y. S. Zhou, S. Lee, Z. L. Wang, *Adv. Funct. Mater.*, 2014, **24**, 2810–2816.
- 31 F.-R. Fan, L. Lin, G. Zhu, W. Wu, R. Zhang, Z. L. Wang, *Nano Lett.*, 2012, **12**, 3109–3114.
- 32 Z.-M. Dang, Y.-H. Lin, C.-W. Nan, *Adv. Mater.*, 2003, **15**, 1625–1629.
- 33 B. Luo, X. Wang, Y. Wang, L. Li, *J. Mater. Chem. A*, 2014, **2**, 510–519.
- 34 Z. Ahmad, M. A. Silaghi, Dielectric material, Intech, 2012, 3–26.
- 35 H. Yu, T. Huang, M. Lu, M. Mao, Q. Zhang, H. Wang, *Nanotechnology*, 2013, **24**, 405401.
- 36 Gregorio, Jr., M. Cestari, *J. Polym. Sci. Part B: Polym. Phys.*, 1994, **32**, 859–870.
- 37 L. Xu, V. Selin, A. Zhuk, J. F. Ankner, S. A. Sukhishvili, S. A. *ACS Macro Lett.*, 2013, **2**, 865–868.
- 38 Z. Hu, M. Tian, B. Nysten, A. M. Jonas, *Nat. Mater.*, 2009, **8**, 62–67.
- 39 S. Satapathy, S. Pawar, P. Gupta, K. Varma, *Bull. Mater. Sci.*, 2011, **34**, 727–733.
- 40 A. Henning, G. Günzburger, R. Jöhr, Y. Rosenwaks, B. Bozic-Weber, C. Housecroft, E. C. Constable, E. Meyer, T. Glatzel, *Beilstein J. Nanotechnol.*, 2013, **4**, 418–428.

CHAPTER 5. FLUORINATED PI BASED POLYMERS

5.1 Introduction

The rapidly increasing demand for intelligent electronic devices, such as portable/wearable devices and sensor networks in the Internet of things (IoT), has triggered considerable interest in triboelectric nanogenerators (TENGs) as renewable and sustainable power sources,¹⁻⁴ owing to their high output power,^{5,6} cost-effectiveness,⁷ and high energy conversion efficiency.⁸⁻¹⁰ The wide-availability and high functionality of TENGs offers itself to several practical applications.¹¹⁻¹⁴

Crucial to the successful implementation of TENGs in practical applications is to generate sufficient output power, usually stored in a capacitor or a battery, to operate the devices.¹⁵⁻¹⁸ Strategies to enhance the output performance of TENGs are generally based on increasing of the transferred charge density between two contacted surfaces, as the electric potential is critically dependent on it.^{19,20} Although the principle of contact-electrification has long been studied,²¹⁻²³ but whose mechanisms are still unclear. Recently, surface-states and electron cloud/potential models have been employed to explain the contact electrification mechanism. However, these models are limited to metal-semiconductors and metal-insulators, i.e.: they are not currently compatible with metal-polymers.^{24,25} Other strategies have relied on the choice of materials in the triboelectric series with electronic and structural modifications, such as a large work-function difference,^{26,27} high porosity,^{28,29} large dielectric constant,^{30,31} and large surface roughness.³²⁻³⁴ The maximum charge density of these TENGs in practical environments, however, requires additional processes, such as artificial charge injection into the dielectric.^{35,36} Recently, several modifications to amplify the current flowing through the external circuit have been successfully demonstrated. Metal-dielectric-metal structures or metal-metal contacts have been introduced and have been proven to increase the charge density of the TENG by several times.^{6,20,37}

Since TENGs are driven by vibrations in the environment and human kinetics, the frequencies of the mechanical forces applied to TENGs are usually random and cannot be tuned naturally.^{38,39} Thus, it is necessary to continuously generate high-output power at a broad range of the frequencies continuously. The amount of charge generated on the surface of the dielectrics also decreases due to the water vapor and charged particles that exist in air. For the generation of sustainable outputs in any environment, it is necessary to develop dielectrics with excellent charge-retention characteristics,^{19,40,41} but there have been few strategies addressing

this material aspect. Thus, a detailed understanding of the charge retention characteristics and further progress in materials design and synthesis technique is necessary for reliable and durable power generation.

In the work described herein, we synthesize polyimide (PI)-based polymers (6FDA-ODA, 6FDA-PDA, and 6FDA-APS) by introducing functionalities (e.g., electron-withdrawing and electron-donating groups) into the backbone. Among them, the TENG based on 6FDA-APS PI, possessing the most negative electrostatic potential and the low-lying lowest unoccupied molecular orbital (LUMO) level, showed superior performances. (i) Its charge density increased by about 7 times compared with that of the commercially available PI (Kapton) film-based one; (ii) Its maximum effective charge density of about $512 \mu\text{C}/\text{m}^2$ under 3 Hz, the highest charge density of TENGs in practical working conditions to the best our knowledge, was obtained without the artificial ion injection process; (iii) Measurement of frequency-dependent output currents showed that its charge density was the largest over the entire frequency range, indicating the best charge-retention characteristics as well as enhanced charge transfer capability of 6FDA-ODA PI; (iv) In addition, a 6FDA-APS-driven sensor network system was also demonstrated, providing the identity of the gases (H_2 , CO , and NO_2) by turning on light-emitting diodes (LEDs) within several seconds.

5.2 Experimental details

5.2.1 Materials

4,4'-(Hexafluoroisopropylidene)diphthalic anhydride (6FDA), 1,4-phenylenediamine (PDA), 4,4'-oxydianiline (ODA), and bis(3-aminophenyl) sulfone (APS) were purchased from Tokyo Chemical Industry Co., Ltd. and used without any further purification. 1-Methyl-2-pyrrolidone (NMP) was purchased from JUNSEI. All solvents were reagent grade, and all reagents were used as received. ^1H NMR was performed in deuterated DMSO, using a 400-MR DD2 (Agilent) 400-MHz spectrometer. The FT-IR spectra were measured with a 670-IR (Agilent) spectrophotometer. The number average molecular weights (M_n) and PDI of the polymer products were determined by gel permeation chromatography (GPC) conducted at 23°C in N,N' -dimethylformamide (DMF) at a flow rate of 1 ml/min, using an Agilent 1260 Infinity GPC system. Monodisperse PS standard (Polymer Laboratories) was used for calibration.

5.2.2 Synthesis of 6FDA-ODA PI, 6FDA-PDA PI, and 6FDA-APS PI through step polymerization

6FDA-ODA PI, 6FDA-PDA PI, and 6FDA-APS PI were helped with synthesis and characterization in the Prof. Yang's laboratory. In a round flask, 6FDA dianhydride monomer (2.25 g, 0.0057 mol) was dissolved in anhydrous N-methyl-2-pyrrolidone (NMP, 16 mL), and purged with argon for 15 min. Diamine co-monomer (1 equiv. of dianhydride) was then added into the solution. The reaction mixture was stirred at 25°C for 24 hours. Afterward, a series of copolyimide films were prepared via a thermal imidization method of the polyamic acid precursors (PAAs) drop-casted films on the glass substrates (2 cm × 2 cm). The imidization was carried out at 250°C for 2 hours under high vacuum.

According to the procedure described above, 6FDA (2.25 g, 5.7 mmol) as dianhydride monomer and ODA (1.01 g, 5.7 mmol) as diamine co-monomer were used for polymerization of 6FDA-ODA. ¹H NMR (400 MHz, DMSO), δ (ppm): 8.20 – 8.05 (br), 7.85 – 7.75 (br), 7.65 – 7.55 (br), 7.40 – 7.30 (br), 7.15 – 7.05 (br). For 6FDA-PDA, 6FDA (2.25 g, 5.7 mmol) as dianhydride monomer and PDA (0.55 g, 5.7 mmol) as diamine co-monomer were used for polymerization. ¹H NMR (400 MHz, DMSO), δ (ppm): 8.20 – 8.10 (br), 7.90 – 7.80 (br), 7.70 – 7.60 (br), 7.50 – 7.40 (br). For 6FDA-APS, 6FDA (2.25 g, 5.7 mmol) as dianhydride monomer and APS (1.26 g, 5.7 mmol) as diamine co-monomer were used for polymerization. ¹H NMR (400 MHz, DMSO), δ (ppm): 8.20 – 8.10 (br), 8.10 – 8.05 (br), 7.95 – 7.85 (br), 7.85 – 7.75 (br), 7.70 – 7.60 (br), 7.60 – 7.55 (br).

5.2.3 Fabrication of PI-based triboelectric nanogenerator

For the PI-based polymer films, the synthesized PAA solutions were drop-coated onto a glass substrate. The PI film was obtained using thermal imidization performed under high vacuum oven at 250°C for 5 hours and cooled at room temperature. After the annealing process, the PI film layer was peeled off from the substrate and the PI films of approximately 150 μm were obtained.

The fabrication of the stretchable electrode was described previously.⁴⁴ Shortly, Ag NWs (Blue Nano, Inc.) and PDMS (Sylgard 184, Dow Corning) were used for the fabrication of stretchable film. For the synthesis of Au NPs, HAuCl₄·3H₂O (30 mL, 30 mM), tetraoctylammonium bromide in toluene (80 mL), and NaBH₄ (25 mL) were used as precursors.

After washing and drying, an aqueous DMAP solution (0.10 M, 50 mL) was added to aliquots (50 mL) of the as-prepared NPs mixtures. The solution was doctor-blade coated onto the electrode's surface at the coating speed of 30 mm/s two times and then the samples were dried at 80°C for 10 min per each coating cycle.

To fabricate the TENG, the spacer between the PI film and the stretchable electrode, which acts as the bottom electrode, was made of four springs with a length of 5 mm in each corner. Finally, the PI-based TENG was obtained. The active area and gap distance of both PVDF and PVDF-Gn films were 2 cm × 2 cm and 1 mm, respectively. A three-layered TENG was also fabricated by adding another stretchable layer underneath the stretchable electrode.

5.2.4 Materials characterization and TENG performances

Morphologies of PI-based films were characterized by a field emission-scanning electron microscope (FE-SEM). The DFT calculations were performed for the electrostatic potential by using Gaussian 09 package with the nonlocal hybrid B3LYP with the 6–31 G* basis set and for charge transfer and LUMO levels by using Vienna ab-initio Simulation package (VASP).^{50,51} We adopted the generalized gradient approximation (GGA) method to describe exchange correlation functional.^{52,53} The pseudopotentials generated under projector augmented wave (PAW) method were used and energy cut-off for planewave basis set was set to 400 eV.^{54,55} The force criteria for optimizing atomic positions was 0.001 eV/Å. The electrode was modelled with six-layered Al (111) slab and the vacuum was set to 20 Å in calculation to avoid interactions between periodic cell. CV was performed using a Solartron electrochemical station (METEK, Versa STAT3) equipped with a three-electrode cell in tetra-n-butylammonium hexafluorophosphate solution in acetonitrile (0.1 M) at a scan rate of 50 mV s⁻¹ under an argon atmosphere at room temperature. A Ag/Ag⁺ electrode, a platinum wire and a glass carbon disk were used as the reference electrode, counter electrode and working electrode, respectively. The LUMO levels of polymers were obtained from the equation $E_{\text{LUMO}}(\text{eV}) = -(E_{(\text{ox})}^{\text{onset}} - E_{(\text{ferrocene})}^{\text{onset}}) + 4.8$. A UV-Vis spectrometer (Perkin-Elmer Lambda 750), equipped with an integrating sphere, was employed to measure the spectral reflectance of the PI films at wavelengths ranging between 300 and 800 nm.

For the measurement of the output voltages and current densities of the TENGs under a vertical compressive stress, a Tektronix DPO 3052 Digital Phosphor oscilloscope and a low-noise current preamplifier (model no. SR570, Stanford Research Systems, Inc.) were used. The

charge density from the output signals was measured using a Keithley 6514 system electrometer. A pushing tester (Labworks Inc., model no. ET-126-4) was used to apply the vertical force to the TENGs.

5.2.5 Fabrication of Gas sensor network systems

The system consists of a two-dimensional 2×2 microarray with ZnO and SnO₂ NPs decorated with metallic (Ag and Pd) NPs, a power unit composed of a TENG and a capacitor, and a main server for the gas recognition. The NPs in sensor were synthesized by a heat-up process. Zinc stearate (2 mmol) and tin (IV) bis (acetylacetonate) dichloride (2 mmol) are used as precursors for ZnO and SnO₂ NPs, respectively. The size distributions of the particles were measured by DLS (Malvern Zetasizer Nano ZS). The NPs were coated on to the interdigitated Ti/Au (20/200 nm) electrodes on SiO₂/Si substrate, followed by rapid thermal annealing at 350°C for 1 min. The sensors were placed in a reaction chamber at 250°C and exposed to pulses of one of three gases (H₂, CO, and NO₂) at various partial pressures entrained in flowing dry air with a flow rate of 2000 sccm. The current measured was measured by using Ivium-n-Stat Multichannel potentiostat (Ivium). The sensing signals were processed by the analog-to-digital converter (ADC) of the STM32L4 micro-controller unit (MCU), transmitted to the main server. By saving the digital value every second, the MCU computed the sensitivity of the gas exposed with the variation of the digital value, compared with the sensitivities of the gases analyzed in PCA. Finally, the gas pattern was classified after matching each gas sensor's sensitivity and the MCU expressed through the LEDs which gas was exposed in this system.

5.3 Results and Discussion

5.3.1 Synthesis of PI-based polymers

PI-based polymers (6FDA-ODA, 6FDA-PDA, and 6FDA-APS) were prepared from a dianhydride monomer of 4,4'-(hexafluoroisopropylidene)diphthalic anhydride (6FDA) and various diamines of 4,4'-oxydianiline (ODA), 1,4-phenylenediamine (PDA), and bis(3-aminophenyl) sulfone (APS) via a two-step method (Figure 23).^{42,43} 6FDA-ODA PI, 6FDA-PDA PI, and 6FDA-APS PI were helped with synthesis and characterization in the Prof. Yang's laboratory. In order to afford the target PI polymers, the corresponding polyamic acid

precursors (PAAs) were first prepared by step-growth polycondensation followed by thermal cyclodehydration (i.e., thermal imidization). Detailed synthetic procedures are provided in Experimental Section.

Step-growth polymerization

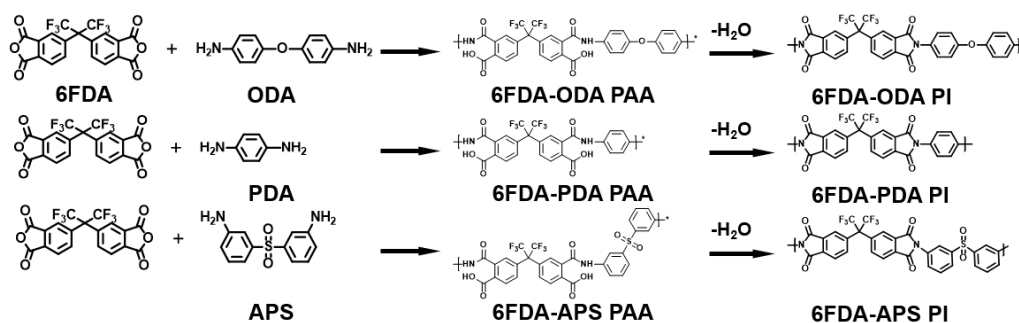


Figure 23. Scheme for the synthesis of polyimides (6FDA-ODA, 6FDA-PDA, and 6FDA-APS) by a two-step method.

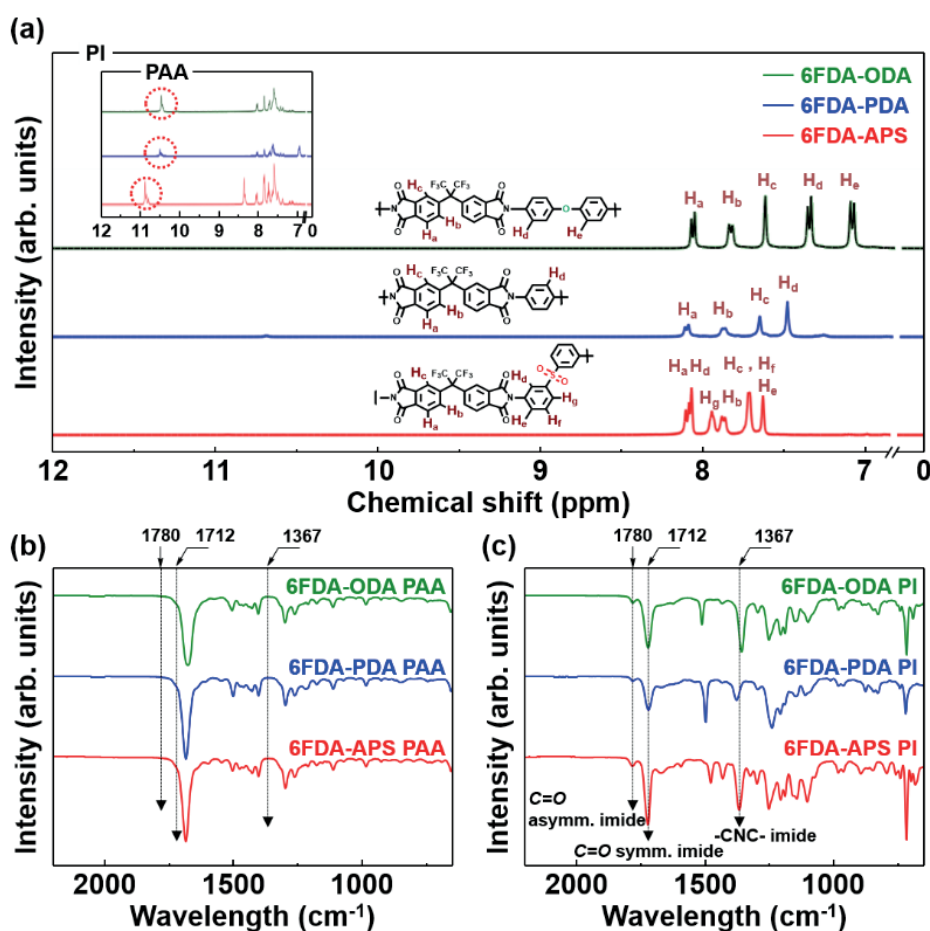


Figure 24. (a) Structures and ^1H NMR spectra of the PI-based Polymers: 6FDA-ODA; 6FDA-PDA; 6FDA-APS. The inset shows ^1H NMR spectra of the PAAs. FT-IR spectra of (b) PAAs and (c) PIs.

The chemical structures of the PAAs and PIs were inspected by the ^1H nuclear magnetic resonance (NMR) and the Fourier-transform infrared (FT-IR) spectroscopy. The complete conversion of PAA to the imide ring was verified by the disappearance of proton peaks from the amide ($-\text{NHCO}-$) at around 10.5 – 11.0 ppm, as displayed in the inset of Figure 24. Besides, the FT-IR spectra of PAAs exhibited broad bands in the range between 3400 cm^{-1} and 3100 cm^{-1} corresponding to O–H and N–H vibration peaks of $-\text{COOH}$ and $-\text{NHCO}-$ groups (Figure 25a) as well as the C=O stretching peaks at 1660 cm^{-1} of the $-\text{NHCO}-$ groups (Figure 24b and 24c). The conversion of PAAs to the imide ring was further corroborated by the appearance of new peaks at 1780 cm^{-1} (asymmetrical C=O stretch), 1712 cm^{-1} (symmetrical C=O stretch), and 1367 cm^{-1} (C–N stretch), together with the dismissal of the broad peaks over 3100 cm^{-1} (O–H and N–H stretch), as shown in Figure 25b.

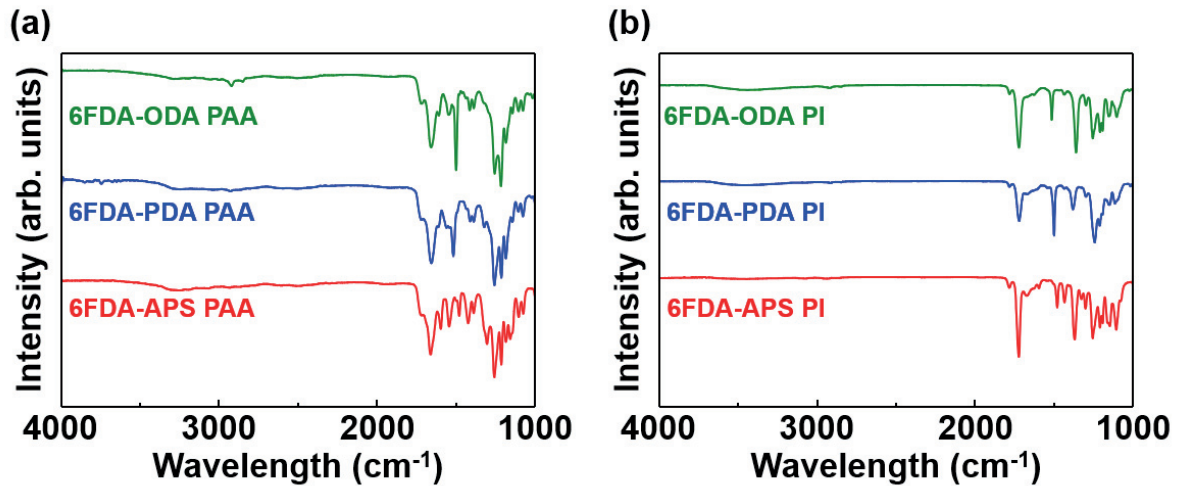


Figure 25. FT-IR spectra of (a) PAAs and (b) PIs: 6FDA-ODA; 6FDA-PDA; 6FDA-APS.

5.3.2 Fabrication of PI based TENGs and its output performance

Preparing high-quality PI films involved the imidization of the PAA precursor films casted from a NMP solvent on glass through thermal treatment at 250°C for 5 hours under vacuum, followed by peeling off them of which process was schematically illustrated in Figure 26a. Interestingly, relative to other PI films, the 6FDA-APS PI film showed far higher transparency (Figure 26b), indicating a much wider optical band gap (E_g^{opt}). For all films, the thickness was fixed to approximately $150\ \mu\text{m}$ and there were almost no pores inside, indicating a negligible compressible effect on the output performance of the TENG-based films. To fabricate the TENG, the peeled-off PI films were then transferred and attached to an Al electrode. A bottom layer was formed with the Ag nanowires embedded PDMS conductive

film decorated by Au nanoparticles. The TENGs have active area of $2\text{ cm} \times 2\text{ cm}$ and gap distance of 1 mm, which was made with four springs with a length of 5 mm in each corner.

The output performances of the TENGs with different polymers were evaluated by a cycled compressive force of around 30 N at an applied frequency of 3 Hz. The open-circuit voltages (V_{oc}) and short-circuit current densities (J_{sc}) of the TENGs were measured (Figure 26c). The TENG based on the commercial product PI (Kapton) as a control reference showed small AC-type electrical output performance of less than 99.7 V and 24.1 mA/m^2 . With a 6FDA-ODA PI film as a dielectric, the V_{oc} and J_{sc} were increased to 137.4 V and 37.2 mA/m^2 respectively, and they further increased to 176.1 V and 45.4 mA/m^2 with the 6FDA-PDA PI film. The highest electrical outputs (with a V_{oc} of 281.6 V and a J_{sc} of 75.1 mA/m^2) were obtained when 6FDA-APS PI film was used, measured under the same mechanical input condition. The instantaneous power was obtained by simultaneously measuring the output voltages and currents (Figure 27) with an external load ranging from $1\text{ M}\Omega$ to $20\text{ M}\Omega$, as shown in Figure 26d. With an external load resistance of $5\text{ M}\Omega$, approximately 2.82 mW was obtained in 6FDA-APS PI-based TENG, a 7-fold enhancement in output power, compared with control reference Kapton-based TENG in Figure 26e and 28. The highest power corresponds to the generated energy per peak of approximately $1.56\text{ }\mu\text{J}$, that is, the generated energy of about $9.3\text{ }\mu\text{W}$ under a frequency of 3 Hz. The generated energy was double that of TENG made of PTFE, widely used in many papers (Figure 26f and 29). The energy conversion efficiency was calculated to be approximately 13.6 % according to the calculation method previously suggested.^{6,44}

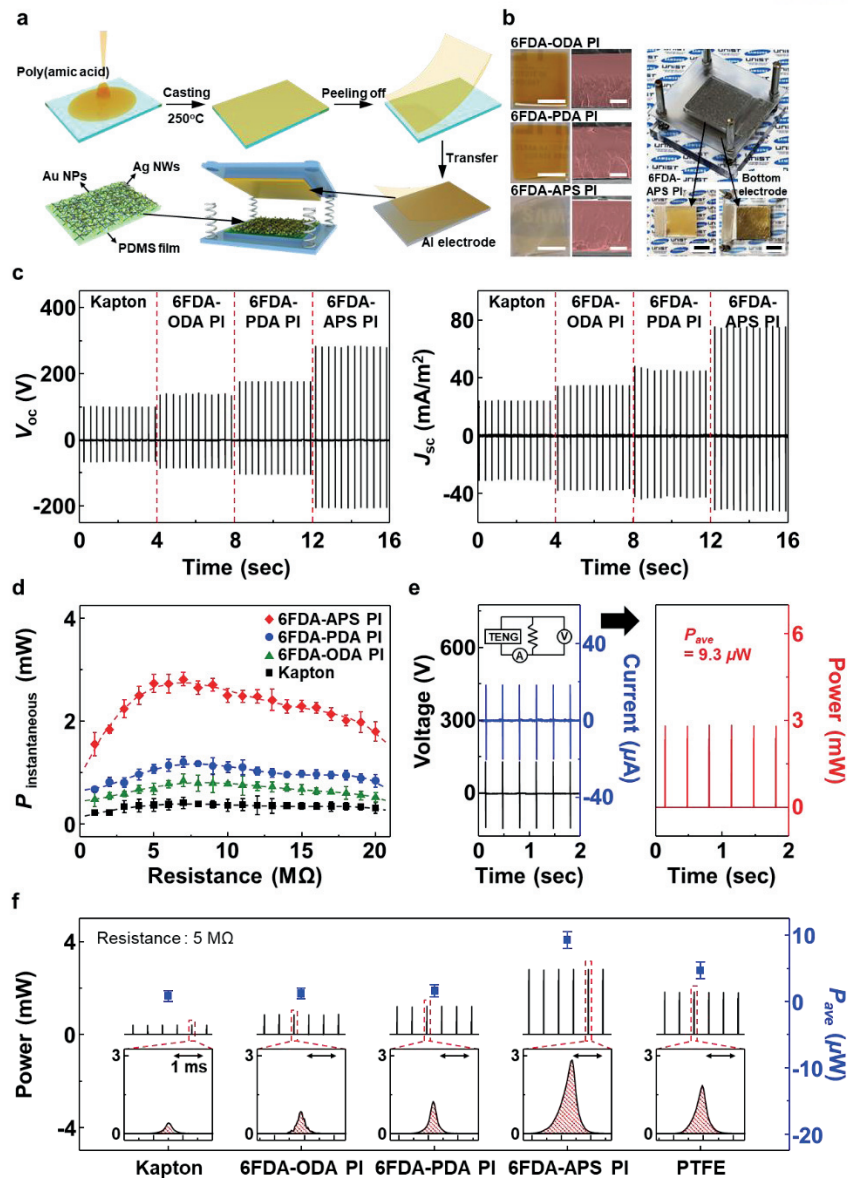


Figure 26. (a) Schematic diagrams of the fabrication process for the PI-based TENGs. (b) Photographs on the left side with scale bars of 1 cm and cross-sectional scanning electron microscope (SEM) images in centre with scale bars of 50 μm of the fluorinated PIs: 6FDA-ODA; 6FDA-PDA; 6FDA-APS. The photograph of the PI-based TENG (consisting of 6FDA-APS film and stretchable electrode) is also shown in right side. Scale bar, 1 cm. (c) The V_{oc} and J_{sc} of the TENGs with different polymers: Kapton; 6FDA-ODA PI; 6FDA-PDA PI; 6FDA-APS PI. (d) The instantaneous power of the PI-based TENG with external loads ranging from 1 M Ω to 20 M Ω . (e) Instantaneous output voltage, current, and power of TENG were measured under 5 M Ω . The generated energy of about 0.1 mW under a frequency of 3 Hz. (f) The instantaneous power and average power ($\mu\text{J/s}$) of the TENGs with different polymers. The inset shows the generated energy per peak.

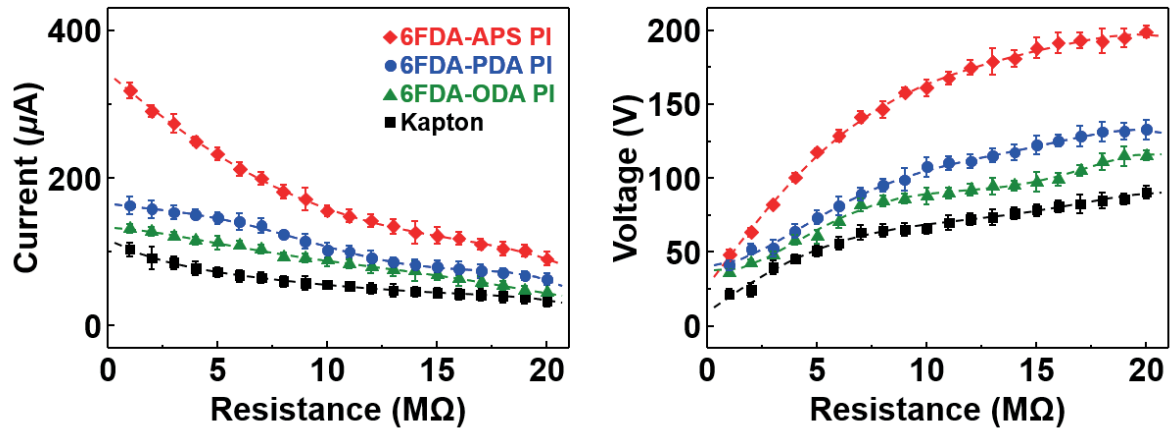


Figure 27. The output current and voltage of the PI-based TENG with an external load ranging from 1 M Ω to 20 M Ω .

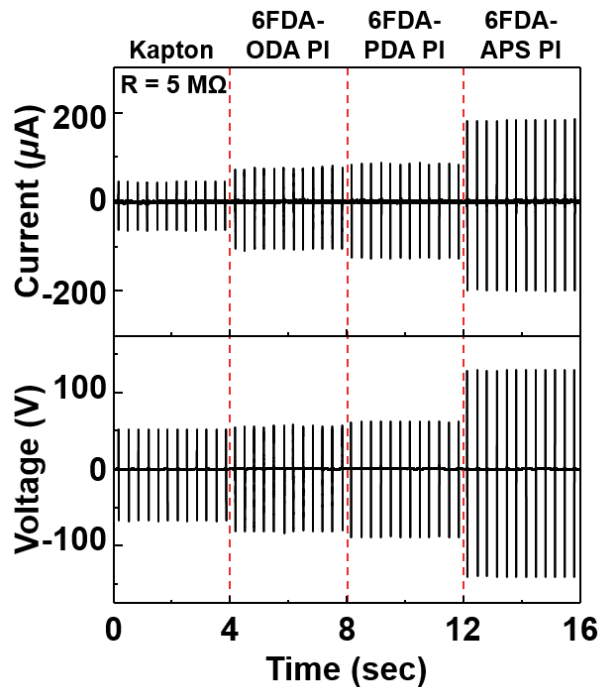


Figure 28. Instantaneous output voltage and current of TENGs with different polymers were measured under 5 M Ω .

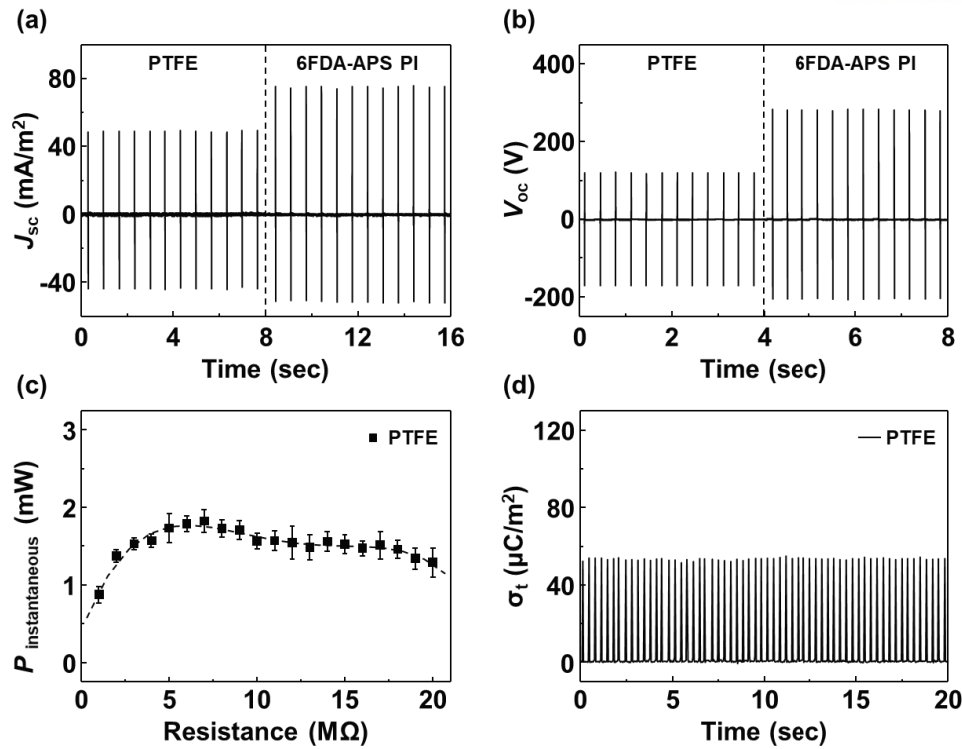


Figure 29. The (a) J_{sc} and (b) V_{oc} of the TENGs with PTFE and 6FDA-APS PI. (c) The instantaneous power of the PTFE-based TENG with an external load ranging from 1 M Ω to 20 M Ω . (d) Charge densities generated by the TENGs with PTFE.

5.3.3 Charge density property of PI based TENGs

The enhancement of the output powers may be explained by the increase of the charge density of the TENGs by using the PI-based polymers. Charge densities (σ_t) of all TENGs were measured under the same mechanical force and frequency. As shown in Figure 30a, the TENG based on Kapton film showed 18.5 μ C/m². For 6FDA-ODA PI film, the σ_t was increased to 26.8 μ C/m². The largest charge density of 101.7 μ C/m² was measured when 6FDA-APS PI film was used, about double of that in the conventional vertical contact-separation mode TENG.³⁵ This suggests that the enhancement in the electrical outputs is ascribed to the increase of the charge density transferred from the electrode.

In order to investigate the reason why the charge density was increased, those of the PI-based film were measured with various input frequencies ranging from 0.05 Hz to 10 Hz (Figure 30b). Charge density is generally determined by the charge-transfer rate between two contacted surfaces and the rate of the charge loss caused by the dissipation of the tribocharges. The frequency dependent study thus shows the charge retention characteristics of the film as

well as the charge transfer capability occurring between two contacted surfaces, i.e.: at low frequencies the charges will dissipate over time, causing a decrease in charge density, while at high frequencies the number of the contacts increases, causing an increase in the total transferred charge density. The charge densities of TENG with 6FDA-APS PI film were the largest among all films ranging over the entire frequency range (Figure 30b). At low frequency of 0.5 Hz (the mean free time between contacts is 19.1 sec in Figure 30c), a charge density of approximately $40 \mu\text{C}/\text{m}^2$ was measured, a tenfold increase from that of the Kapton film. The 6FDA-APS PI film, in other words, can retain the most charges via contact electrification. As the frequency increased to 10 Hz, the charge density increased to $111.8 \mu\text{C}/\text{m}^2$. It is also worth noting that the increase of the charge densities of the TENGs with 6FDA-APS PI film was greater as the frequency increased, compared with others. This indicates that charge transfer is most efficient in the film, suggesting that the transferred charges are strongly trapped in the 6FDA-APS PI film with the best charge-transfer capability.

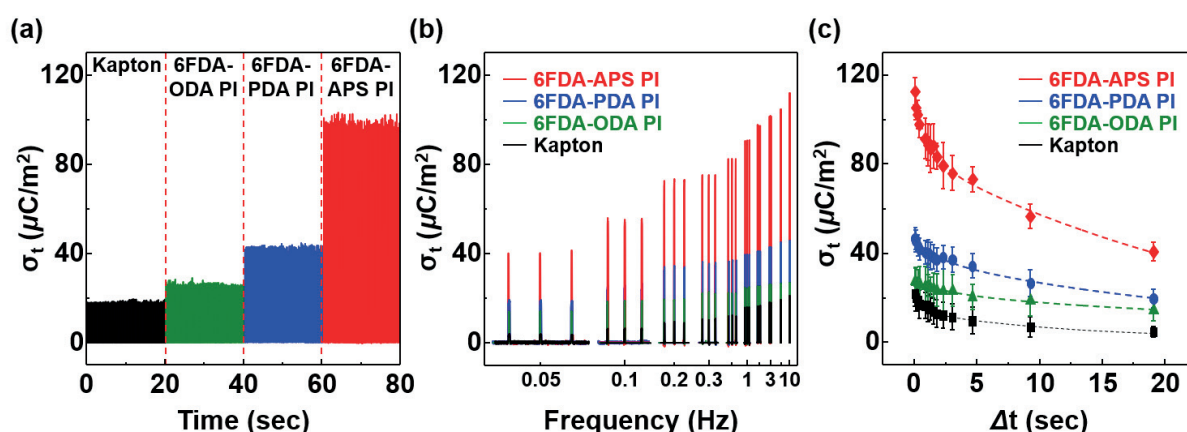


Figure 30. (a) Charge densities generated by the TENGs with different polymers: Kapton; 6FDA-ODA PI; 6FDA-PDA PI; 6FDA-APS PI. The charge densities with the PI-based films as a function of (b) the input frequencies ranging from 0.05 to 10 Hz and (c) the mean free times between the contacts ranging from 0.1 to 19.1 sec.

5.3.4 Electrostatic potential maps of the fluorinated PIs

To access the molecular electrostatic potential and the charge distribution depending on dipole moments, partial charges, electronegativity, and the site of chemical reactivity, the charge retention characteristics of the PI films as a function of the functional groups were investigated with density functional theory (DFT) calculations (Gaussian 09 package with the

nonlocal hybrid Becke three-parameter Lee-Yang-Parr (B3LYP) function and the 6-31 G*). The potential maps of Figure 31 shows that the ether (–O–) and sulfone (–SO₂–) groups shows a main contributor to the variation of the electrostatic potential in the molecular structures. In particular, the –SO₂– groups showed the most negative electrostatic potential, even lower than that of the fluoride (F) region. This suggests that –SO₂– groups play a significant role as the electron-withdrawing group in capturing the charges transferred from the Al electrodes, which accounts for the highest charge density on the surface of the 6FDA-APS PI film.

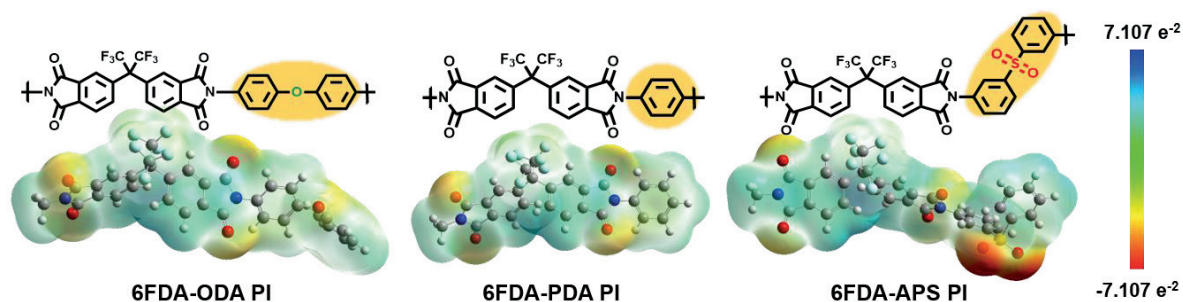


Figure 31. Electrostatic potential maps of the fluorinated PIs: 6FDA-ODA; 6FDA-PDA; 6FDA-APS.

5.3.5 DFT calculation

We further conducted DFT calculations to investigate the origin of the difference in the charging efficiency among the polymers. At first, we calculated the energy barrier in the charge transfer process from Al to polymers to compare the efficiency of the charge transfer. Figure 32a shows LUMO levels of three polymers up to LUMO+5, of which energy levels are aligned with respect to vacuum level. The 6FDA-APS PI has significantly lower LUMO energy levels than the other polymers (6FDA-ODA PI and 6FDA-PDA PI), and hence 6FDA-APS PI would be superior to the other two polymers in charge transfer. Figure 32b shows electrostatic planar average potentials of three polymers, where the end-group of monomer is located at 2.5 Å above the Al (111) surface. The energy barrier heights, which are based on the Fermi energy level of Al (111), of 6FDA-ODA PI, 6FDA-PDA PI, and 6FDA-APS PI are 1.97, 1.75, and 1.10 eV, respectively. It indicates that charges are most easily transferred from electrode to 6FDA-APS PI among the polymers. The output powers measured from experiments were plotted in terms of energy barriers and LUMO levels from DFT calculations in Figure 32c. The DFT calculation results clearly support experimental result that 6FDA-APS PI shows highest charging efficiency.

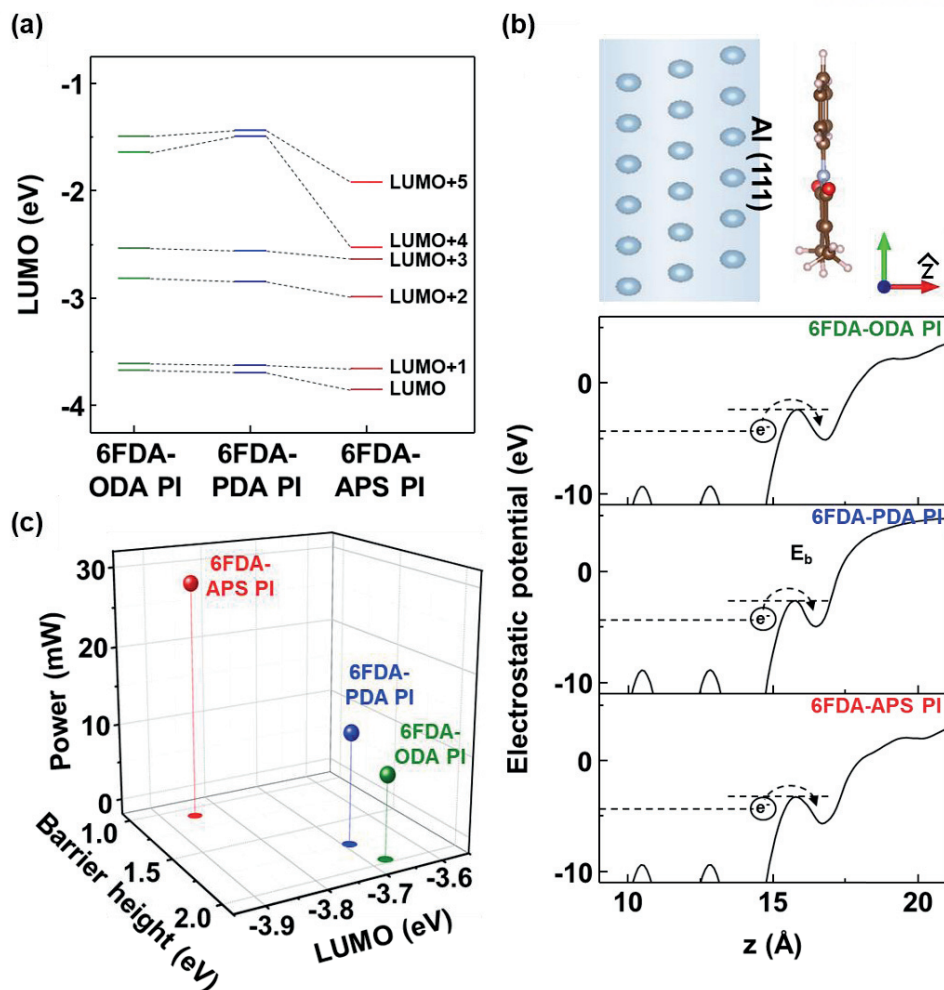


Figure 32. (a) Energy diagram of three monomers, of which energy levels are aligned with respect to vacuum energy level, between LUMO and LUMO+5. (b) Electrostatic planar average potentials and the corresponding energy barrier heights for electron transfer from Al electrode to monomers. (c) The output powers of the PI-based TENGs with barrier height and LUMO level.

5.3.6 Energy levels of PI-based films

In order to determine the LUMO energy levels of PI-based films, we conducted cyclic voltammetry (CV) plotted in Figure 33a. The LUMO levels were calculated from the redox onset potentials in CV data according to the equations of $E_{\text{LUMO}} = -e(E_{\text{red}})^{\text{onset}} + 4.8$ - redox potential of ferrocene/ferrocenium (F_c/F_c⁺) couple) (eV). Among them, the 6FDA-APS PI shows the low-lying LUMO, being in a good agreement with the above simulation results. Besides, as shown in Figure 33b, the 6FDA-APS PI reaches absorption peak in the only small

wavelength range below 400 nm, resulting in the largest E_g^{opt} , and ultimately yielding high transmittance, being consistent with the optical image displayed in Figure 26b. In contrast, other samples, including the Kapton, exhibited wider E_g^{opt} s and poor transmittance. These results indicate that for 6FDA-APS PI, the charge transfer complexes (CTCs) are suppressed, attributable to a combination of two electron-withdrawing groups (trifluoromethyl ($-\text{CF}_3$) and $-\text{SO}_2-$ groups) in the backbone, whereas occurring the CTC behaviors in other samples including Kapton.

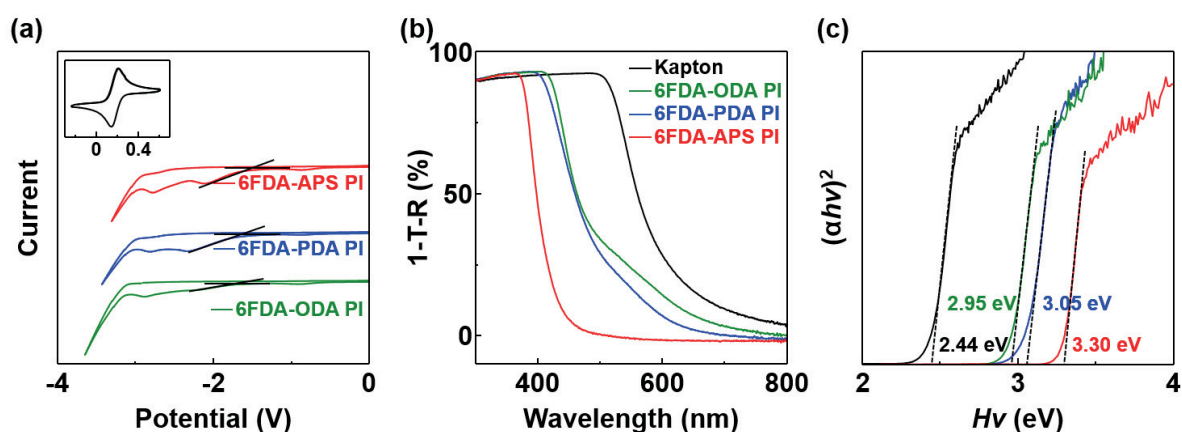


Figure 33. (a) Cyclic voltammetry of the fluorinated PIs: 6FDA-ODA; 6FDA-PDA; 6FDA-APS. (b) UV-vis absorption spectra in the range from 300 to 800 nm. (c) Corresponding plot of transformed Kubelka–Munk function versus the energy of the light.

Since no oxidation peaks were detected within the operating window ($\pm 2\text{V}$) during the anodic sweep of the CV measurement, we determined highest occupied molecular orbital (HOMO) levels by transforming the absorbance by the following equation for the near-edge absorption known as the Kubelka-Munk method, plotted in Figure 33c.⁴⁵

$$(\alpha hv)^2 = hv - E_g^{\text{opt}} \quad (11)$$

where α is the absorption coefficient and hv is the photon energy. The E_g^{opt} of Kapton, 6FDA-ODA PI, 6FDA-PDA PI, and 6FDA-APS PI films which is determined from the intercept of the tangents to the plots of $(\alpha hv)^2$ vs the photon energy are 2.44 eV, 2.95 eV, 3.05 eV, and 3.30 eV, respectively. HOMO levels were estimated based on these results, whereas the LUMO levels were calculated from $E_{\text{LUMO}} = E_{\text{HOMO}} + E_g^{\text{opt}}$. HOMO levels are thus 6.62 eV, 6.62 eV, and 7.15 eV for 6FDA-ODA PI, 6FDA-PDA PI, and 6FDA-APS PI films, respectively. Although the charge neutrality level should be experimentally determined, simultaneously lowering the LUMO and HOMO levels and increasing the E_g^{opt} s reflects its decrease, implying

more efficient charge transfer in 6FDA-APS PI than others. The 6FDA-APS PI film was also used in three-layered TENG as a dielectric and the charge density was measured, compared with the TENG fabricated with PTFE film (Figure 34a). Under a compressive force of 30 N and a frequency of 3 Hz, the maximum charge density of approximately $250 \mu\text{C}/\text{m}^2$ was measured in TENG fabricated with PTFE film, which was reported before.^{6,44} The increase of the charge density is attributable to the sequential contact configuration of the TENG and ground connection of the middle layer. The 6FDA-APS PI film increased the charge density by about 2 times to $512 \mu\text{C}/\text{m}^2$ under 3 Hz, the highest charge density of TENGs in practical working conditions without additional ions injection and circuitry to increase further the charge density to the best our knowledge (Figure 34b).

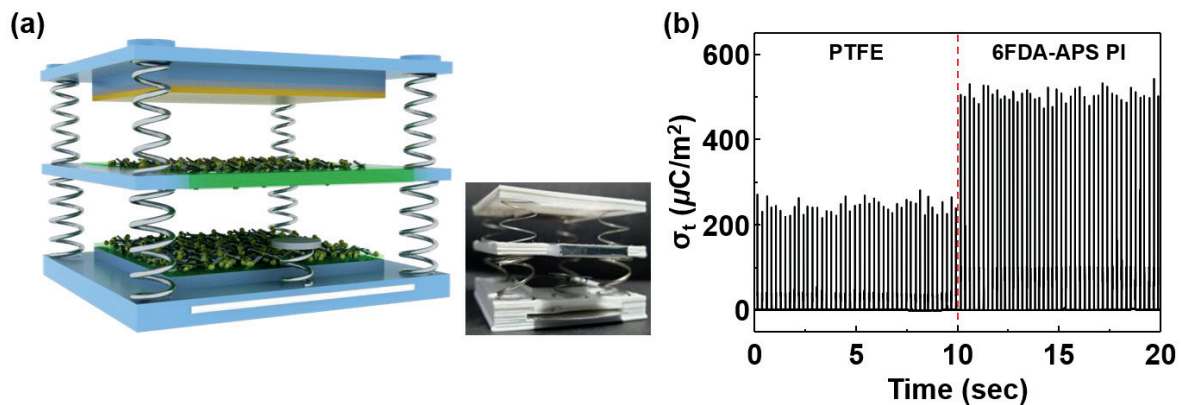


Figure 34. (a) Schematic diagrams and the photograph of the 6FDA-APS PI film-based three-layered TENG. (b) Charge densities generated by the TENG fabricated with PTFE film and 6FDA-APS PI film.

5.3.7 Sensor network system driven by a TENG

Finally, we demonstrated a sensor network system driven by a TENG fabricated with the 6FDA-APS PI film (Figure 35a). The system consists of a two-dimensional 2×2 microarray with ZnO and SnO₂ nanoparticles decorated with metallic (Ag and Pd) nanoparticles, a power unit composed of a TENG and a capacitor, and a main server for the gas recognition. In the sensor, the ZnO and SnO₂ nanoparticles were synthesized by a heat-up process, and the average sizes of the nanoparticles were about 43 and 48 nm, respectively, as measured by dynamic light scattering (DLS) (Figure 36). The Ag and Pd films were deposited on the nanoparticles by using electron beam evaporation, followed by rapid thermal annealing at 300°C, which produced well-covered nanoparticles. The power unit has the converting

circuit consisted of a rectifier, three low-voltage capacitors ($3 \times 0.001 \mu\text{F}$), and an electrolytic capacitor ($10 \mu\text{F}$). The analog signals obtained in the sensors were processed by the analog-to-digital converter (ADC) of the STM32L4 micro-controller unit (MCU) to be transmitted to the main server for pattern recognition. When a vertical compressive force of 30 N under a frequency of 1 Hz was applied to the TENG, a $10\text{-}\mu\text{F}$ capacitor was charged up to approximately 0.79 V within 10 minutes. As the frequency increased to 3 Hz, the charged voltage increased to 1.71 V, enough to supply continuous power to each sensor element of the array at the same time, although there was a small reduction in the voltage when the switch to sensors was turned on (Figure 35b). Further increase in the frequency to 10 Hz, it reached to 3.16 V. This indicates that stable power can be supplied to the sensors at broad range of the frequencies continuously.

Figure 35c shows the change in currents of each sensor toward the three gases as a function of gas concentration from 5 ppm to 100 ppm, measured at 250°C . For Pd-decorated ZnO nanoparticles, adding each of the two reducing gases (H_2 and CO) to the air stream caused the current to increase in less than 1 min, returning to its initial value reversibly when the gases are shut off. The gas molecules were known to be dissociated on the Pd nanoparticle surface, followed by a fast diffusion into the metal oxides, increasing the sensitivities.⁴⁶ In contrast, NO_2 gas increased the current when the film was exposed to the gases. The measured S values of Pd-ZnO with the flow rate of 100 ppm were 1.62, 0.49, and -1.82 for H_2 , CO, and NO_2 , respectively. For the Ag-decorated ZnO, the measured S values were 0.58, 0.19, and -0.85 for H_2 , CO, and NO_2 , respectively, explained via electron transport across the interfaces between the Ag and the ZnO.⁴⁷ In case of SnO_2 nanoparticles, the sensitivities toward the gases were lower than those of ZnO nanoparticles-based sensors, may be explained by the low surface-to-volume ratio of the SnO_2 nanoparticles. Based on these results, the aggregate data set was processed using principal component analysis (PCA) and plotted as three-dimensional maps to indicate the extent to which the analysis could separate the response to the three gases into separate classes (Figure 35d). PCA was performed using singular value decomposition method with the MATLAB program. The sensor responses produced the feature clusters among the three gases at 95% confidence level. That is, the three gases— H_2 , CO, and NO_2 —would be identified unequivocally by the sensor described here, in gaseous samples each containing one of the three test gases mixed in air.

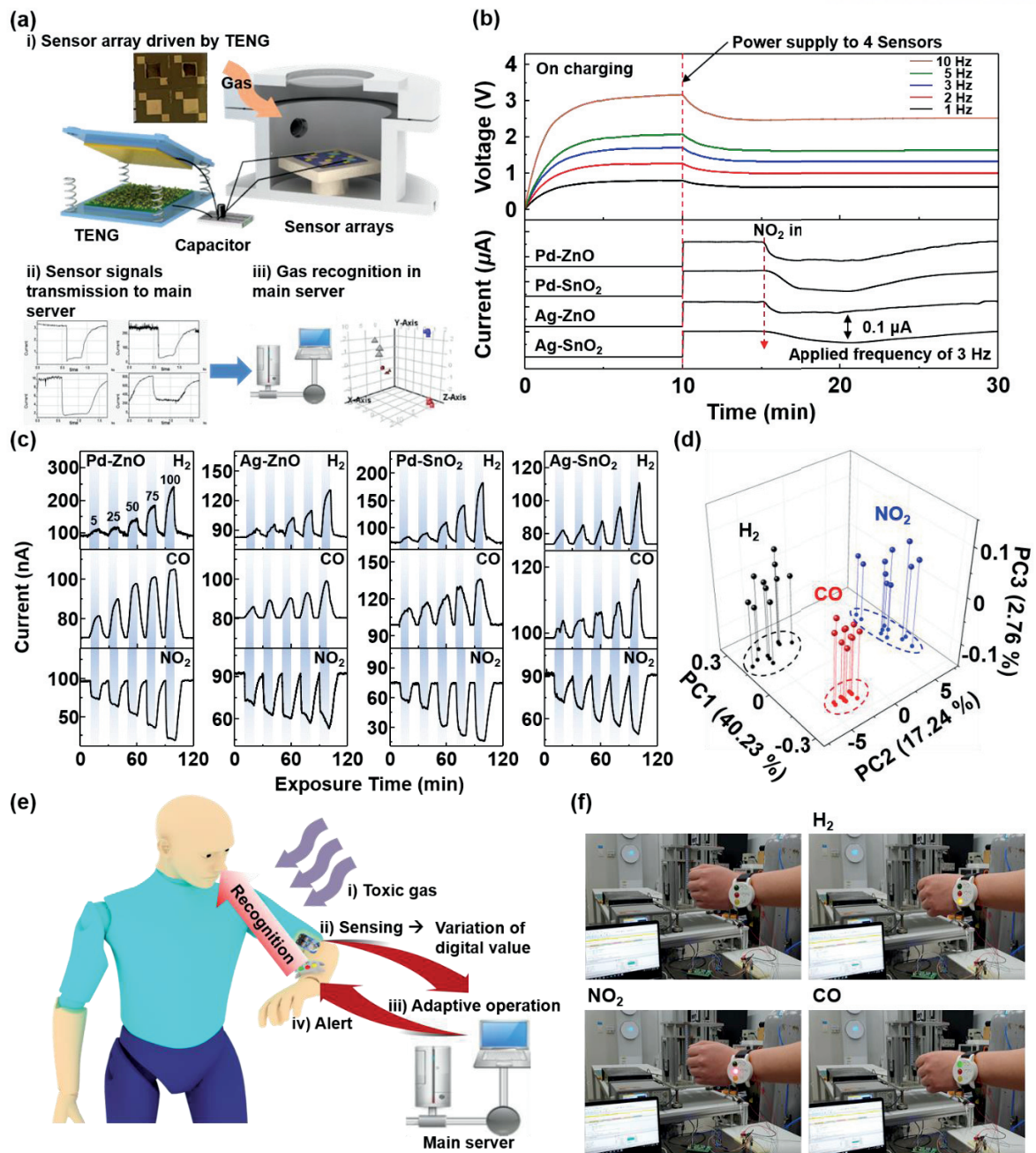


Figure 35. (a) Schematic diagram of the gas sensor network system driven by the 6FDA-APS PI film-based TENG. (b) The charging curves of the 10- μ F capacitor by the TENG before and after NO₂ exposure as a function of input frequencies and the corresponding change in currents changes of 4 sensors with the NO₂. (c) The change in currents of each sensor toward the three gases (H₂, CO, and NO₂) as a function of gas concentration from 1 ppm to 100 ppm, measured at 250°C. (d) Principal component analysis, plotted as three-dimensional maps. (e) Conceptual schematic diagram of the self-powered sensor network systems. (f) The photographs of the lit LEDs; Yellow (H₂), Red (NO₂), and Green (CO).

With the selective sensing performance of the sensor driven by the TENG, a sensor network system was demonstrated by exposing the sensors to the gases (Figure 35e). The signals were immediately transmitted to the main server in the form of value changes over the time. The MCU computed the sensitivity of the gas exposed with the variation of the digital value, compared with the sensitivities of the gases analyzed in PCA, making it possible to identify the gas after the matching process and turning on the LEDs expressed by the MCU (Figure 37). The overall process was described in Figure 38. Within 3 – 6 seconds, the gases were identified by the LEDs; Yellow (H_2), Red (NO_2), and Green (CO), as shown in Figure 35f and 39. Although the operating temperature of the sensor was reached by an external power source, it is believed that the power required to maintain the sensors at the high temperature can decrease to several μW .⁴⁸ Wireless transmission of the sensor signals can be also realized in near future because the power consumption of the Bluetooth transmitter decreases down to several mW and further decrease can be expected soon.⁴⁹ Thus, this demonstration shows the meaningfulness of the sensor network systems driven by a TENG operating under practical environments.

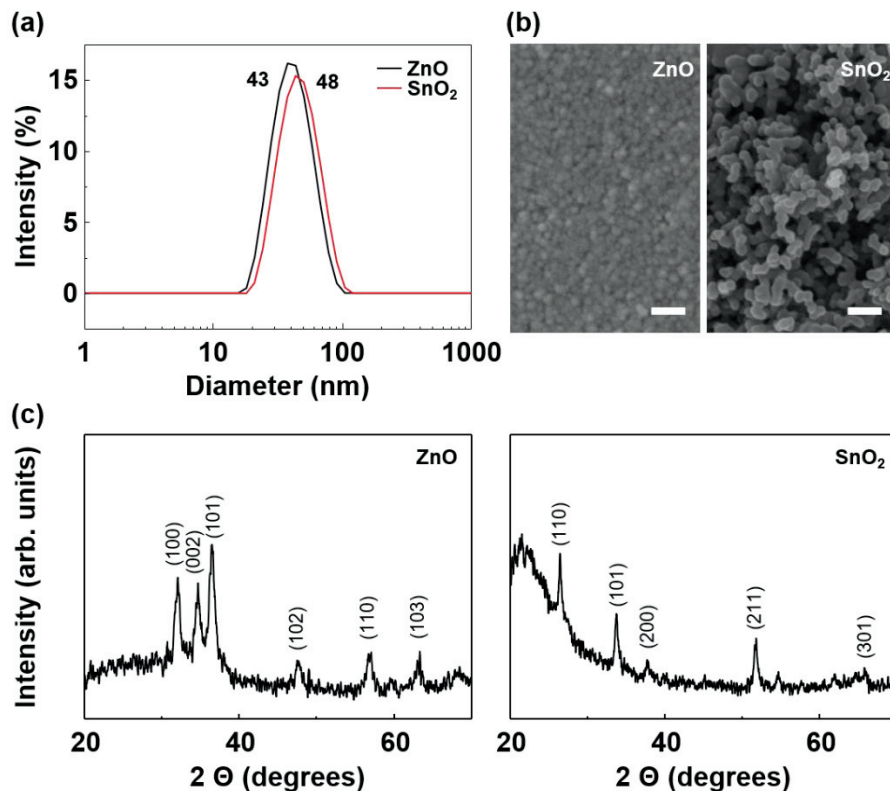


Figure 36. (a) Size distribution via dynamic light scattering (DLS) for ZnO and SnO₂ nanoparticles. (b) SEM images of ZnO and SnO₂ nanoparticles with scale bars of 100 nm. (c) X-ray diffraction (XRD) patterns of ZnO and SnO₂ nanoparticles.

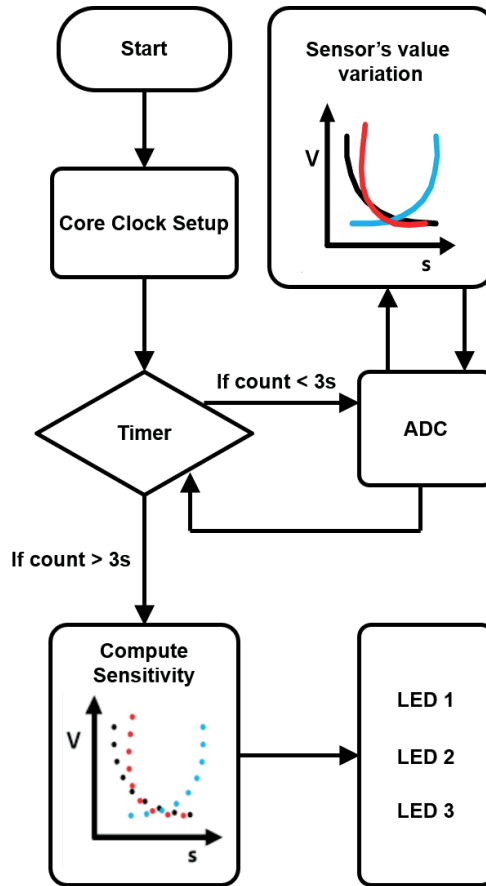


Figure 37. Flow chart of the gas identity algorithm.

Sensor network system

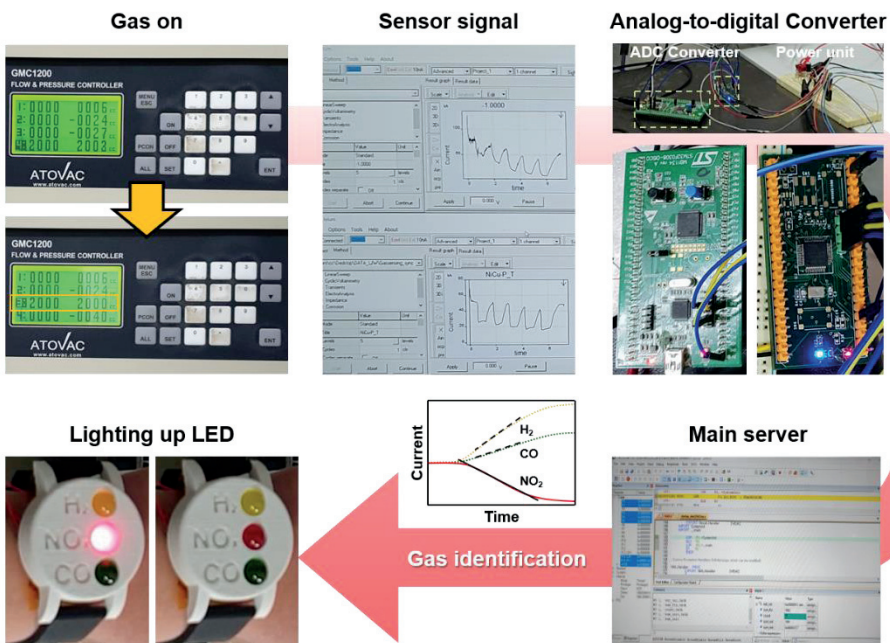


Figure 38. Systematic configuration of the self-powered sensor network system.

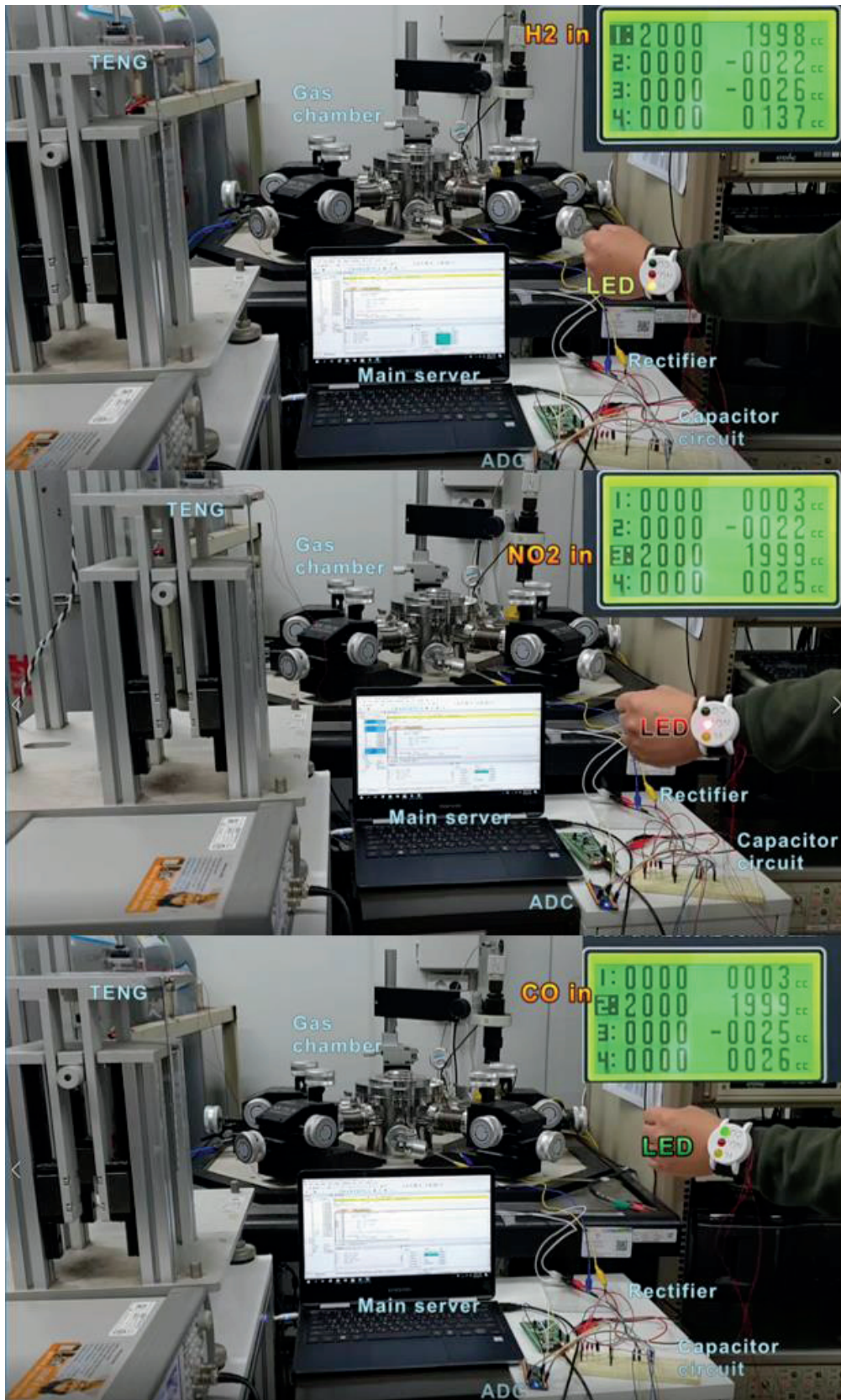


Figure 39. The captured images from Supplementary movie 1, 2, and 3 showing the H₂, NO₂, and CO gas identification of sensor network system.

5.4 Conclusion

In summary, we have synthesized various PI-based polymers (6FDA-ODA, 6FDA-PDA, and 6FDA-APS) by introducing functionalities (e.g., electron-withdrawing and electron-donating groups) into the backbone in order to fabricate high-output triboelectric nanogenerators. Density functional theory calculations showed that among the polymers, the 6FDA-APS PI possessed the most negative electrostatic potential and the low-lying LUMO level, supported by the measurement of the optical properties and the cyclic voltammetry of the films. This finding explains the frequency-dependent output currents, showing that its charge density was the largest ranging over the entire frequency range and the best charges retention characteristics as well as enhanced charge transfer capability. The charge density significantly increased by about 7 times compared with that of the commercially available PI (Kapton) film-based one. The maximum effective charge density of about $512 \mu\text{C}/\text{m}^2$ under 3 Hz was obtained without any ion injection process and additional circuitry, which is the highest charge density of TENGs in practical working conditions to the best our knowledge. Finally, a 6FDA-APS-driven sensor network system consisting of 2×2 sensor arrays composed of ZnO and SnO₂ nanoparticles was demonstrated, providing the identity of the gases (H₂, CO, and NO₂) by turning on LEDs within several seconds.

5.5 References

- 1 G. Zhu, Z.-H. Lin, Q. Jing, P. Bai, C. Pan, Y. Yang, Y. Zhou and Z. L. Wang, *Nano Lett.*, 2013, **13**, 847-853.
- 2 J. Chen, G. Zhu, W. Yang, Q. Jing, P. Bai, Y. Yang, T.-C. Hou and Z. L. Wang, *Adv. Mater.*, 2013, **25**, 6094-6099.
- 3 W. Du, X. Han, L. Lin, M. Chen, X. Li, C. Pan and Z. L. Wang, *Adv. Energy Mater.*, 2014, **4**, 1301592.
- 4 W. Yang, J. Chen, G. Zhu, J. Yang, P. Bai, Y. Su, Q. Jing, X. Cao and Z. L. Wang, *ACS Nano*, 2013, **7**, 111317-11324.
- 5 G. Zhu, Y. S. Zhou, P. Bai, X. S. Meng, Q. Jing, J. Chen and Z. L. Wang, *Adv. Mater.*, 2014, **26**, 3788-3796.
- 6 J. Chun, B. U. Ye, J. W. Lee, D. Choi, C.-Y. Kang, S.-W. Kim, Z.L. Wang and J. M. Baik, *Nat. Commun.*, 2016, **7**, 12985.
- 7 Z. L. Wang, J. Chen and L. Lin, *Energy Environ. Sci.*, 2015, **8**, 2250-2282.
- 8 W. Tang, T. Jiang, F. R. Fan, A. F. Yu, C. Zhang, X. Cao and Z. L. Wang, *Adv. Funct. Mater.*, 2015, **25**, 3718-372.
- 9 L. Lin, Y. Xie, S. Niu, S. Wang, P.-K. Yang and Z. L. Wang, *ACS Nano*, 2015, **9**, 922-930.
- 10 Y. Zi, J. Wang, S. Wang, S. Li, Z. Wen, H. Guo and Z. L. Wang, *Nat. Commun.*, 2016, **7**, 10987.
- 11 G. Zhu, W. Q. Yang, T. Zhang, Q. Jing, J. Chen, Y. S. Zhou, P. Bai and Z. L. Wang, *Nano Lett.*, 2014, **14**, 3208-3213.
- 12 S. Park, H. Kim, M. Vosgueritchian, S. Cheon, H. Kim, J. H. Koo, T. R. Kim, S. Lee, G. Schwartz, H. Chang and Z. Bao, *Adv. Mater.*, 2014, **26**, 7324-7332.
- 13 X. Pu, M. Liu, X. Chen, J. Sun, C. Du, Y. Zhang, J. Zhai, W. Hu and Z. L. Wang, *Sci. Adv.*, 2017, **3**, e1700015.
- 14 Z. Lin, J. Chen, X. Li, Z. Zhou, K. Meng, W. Wei, J. Yang and Z. L. Wang, *ACS Nano*, 2017, **11**, 8830-8837.
- 15 X. Pu, M. Liu, L. Li, C. Zhang, Y. Pang, C. Jiang, L. Shao, W. Hu and Z. L. Wang, *Adv. Sci.*, 2016, **3**, 1500255.
- 16 X. Liu, K. Zhao, Z. L. Wang, Y. Yang, *Adv. Energy Mater.*, 2017, **7**, 1701629.

- 17 X. Cheng, L. Miao, Y. Song, Z. Su, H. Chen, X. Chen, J. Zhang, H. Zhang, *Nano Energy*, 2017, **38**, 438-446.
- 18 H. Ryu, J. H. Lee, U. Khan, S. S. Kwak, R. Hinchet and S.-W. Kim, *Energy Environ. Sci.*, 2018, **11**, 2057-2063.
- 19 J. Wang, C. Wu, Y. Dai, Z. Zhao, A. Wang, T. Zhang and Z. L. Wang, *Nat. Commun.*, 2017, **8**, 88.
- 20 L. Cheng, Q. Xu, Y. Zheng, X. Jia and Y. Qin, *Nat. Commun.*, 2018, **9**, 3773.
- 21 J. Lowell, *J. Phys. D: Appl. Phys.*, 1975, **8**, 53-63.
- 22 W. R. Harper, *Proc. R. Soc. A*, 1951, **205**, 83-103.
- 23 C. B. Duke and T. J. Fabish, *J. Appl. Phys.*, 1978, **49**, 315-321.
- 24 J. Wu, X. Wang, H. Li, F. Wang, W. Yang and Y. Hu, *Nano Energy*, 2018, **48**, 607-616.
- 25 C. Xu, Y. Zi, A. C. Wang, H. Zou, Y. Dai, X. He, P. Wang, Y.-C. Wang, P. Feng, D. Li and Z. L. Wang, *Adv. Mater.*, 2018, **30**, 1706790.
- 26 P. Bai, G. Zhu, Y. S. Zhou, S. Wang, J. Ma, G. Zhang and Z. L. Wang, *Nano Res.*, 2014, **7**, 990-997.
- 27 Y. S. Zhou, S. Wang, Y. Yang, G. Zhu, S. Niu, Z.-H. Lin, Y. Liu, Z. L. Wang, *Nano Lett.*, 2014, **14**, 1567-1572.
- 28 J. Chun, J. W. Kim, W.-s. Jung, C.-Y. Kang, S.-W. Kim, Z. L. Wang and J. M. Baik, *Energy Environ. Sci.*, 2015, **8**, 3006-3012.
- 29 Q. Zheng, L. Fang, H. Guo, K. Yang, Z. Cai, M. A. B. Meador and S. Gong, *Adv. Funct. Mater.*, 2018, **28**, 1706365.
- 30 W. Seung, H.-J. Yoon, T. Y. Kim, H. Ryu, J. Kim, J.-H. Lee, J. H. Lee, S. Kim, Y. K. Park, Y. J. Park and S.-W. Kim, *Adv. Energy Mater.*, 2017, **7**, 1600988.
- 31 J. W. Lee, H. J. Cho, J. Chun, K. N. Kim, S. Kim, C. W. Ahn, I. W. Kim, J.-Y. Kim, S.-W. Kim, C. Yang and J. M. Baik, *Sci. Adv.*, 2017, **3**, e1602902.
- 32 X.-S. Zhang, M.-D. Han, R.-X. Wang, F.-Y. Zhu, Z.-H. Li, W. Wang and H.-X. Zhang, *Nano Lett.*, 2013, **13**, 1168-1172.
- 33 C. K. Jeong, K. M. Baek, S. Niu, T. W. Nam, Y. H. Hur, D. Y. Park, G.-T. Hwang, M. Byun, Z. L. Wang, Y. S. Jung and K. J. Lee, *Nano Lett.*, 2014, **14**, 7031-7038.
- 34 S. Wang, L. Lin and Z. L. Wang, *Nano Lett.*, 2012, **12**, 6339-634.
- 35 S. Wang, Y. Xie, S. Niu, L. Lin, C. Liu, Y. S. Zhou and Z. L. Wang, *Adv. Mater.*, 2014, **26**, 6720-6728.

- 36 T. Zhou, L. Zhang, F. Xue, W. Tang, C. Zhang and Z.L. Wang, *Nano Res.*, 2016, **9**, 1442-1451.
- 37 L. Xu, T. Z. Bu, X. D. Yang, C. Zhang and Z.L. Wang, *Nano Energy*, 2018, **49**, 625-633.
- 38 J. Yang, J. Chen, Y. Yang, H. Zhang, W. Yang, P. Bai, Y. Su and Z. L. Wang, *Adv. Energy Mater.*, 2014, **4**, 1301322.
- 39 J. Chen and Z.L. Wang, *Joule*, 2017, **1**, 480-521.
- 40 Y. Zi, C. Wu, W. Ding and Z. L. Wang, *Adv. Funct. Mater.*, 2017, **27**, 1700049.
- 41 N. Cui, L. Gu, Y. Lei, J. Liu, Y. Qin, X. Ma, Y. Hao and Z. L. Wang, *ACS Nano*, 2016, **10**, 6131-6138.
- 42 A. Ghosh, S. K. Sen, S. Banerjee and B. Voit, *RSC Adv.*, 2012, **2**, 5900-5926.
- 43 E. Park, J. Seo, H. Han, H. Kim and Y. Kim, *Adv. Sci.*, 2018, **5**, 1800331.
- 44 J. P. Lee, J. W. Lee, B.-K. Yoon, H. J. Hwang, S. Jung, K. A. Kim, D. Choi, C. Yang and J. M. Baik, *Nano Energy*, 2019, **56**, 571-580.
- 45 J. P. Perdew, K. Burke and M. Ernzerhof, *Phys. Rev. Lett.*, 1996, **77**, 3865-3868.
- 46 J. P. Perdew, K. Burke and M. Ernzerhof, *Phys. Rev. Lett.*, 1997, **78**, 1396.
- 47 G. Kresse and J. Hafner, *Phys. Rev. B*, 1993, **47**, 558-561.
- 48 G. Kresse and J. Hafner, *Phys. Rev. B*, 1994, **49**, 14251-14269.
- 49 P.E. Blöchl, *Phys. Rev. B*, 1994, **50**, 17953-17979.
- 50 G. Kresse and D. Joubert, *Phys. Rev. B*, 1999, **59**, 1758-1775.
- 51 Y. P. Xie, Z. B. Yu, G. Liu, X. L. Ma and H.-M. Cheng, *Energy Environ. Sci.*, 2014, **7**, 1895-1901.
- 52 C. Wang, L. Yin, L. Zhang, D. Xiang and R. Gao, *Sensors*, 2010, **10**, 2088-2106.

CURRICULUM VITAE

Jae Won Lee

Street Address: UNIST-gil 50, Eonyang-eup, Ulju-gun, Ulsan, Republic of Korea, 44919.
E-mail: leejw@unist.ac.kr / titireto@gmail.com · Phone: +82-10-5307-7680

EDUCATION

- 2014-2019 **Ulsan National Institute of Science and Technology (UNIST)**
- Ph.D in Materials Science and Engineering.
 - Supervisor: Professor, Jeong Min Baik
- 2009-2014 **Ulsan National Institute of Science and Technology (UNIST)**
- B.S. in Materials Science and Engineering
-

TEACHING EXPERIENCE

Teaching Assistant

- 2014, Spring **Teaching Assistant, Thermodynamics of Materials**, Department of Materials Science and Engineering, Ulsan National Institute of Science and Technology
- 2014, Fall **Teaching Assistant, Introduction to Semiconductor**, Department of Materials Science and Engineering, Ulsan National Institute of Science and Technology

Mentoring

- 2013~2014 **Ulsan Gang Nam High School**, Advised four high school students on independent research projects
- Training support provided by: 2013 UNIST-Science High School R&E Program
 - Thesis: The Synthesis and Photocatalytic Characterization of TiO₂ Nanorods by a Hydrothermal Method.
-

HONORS

- 2016 • **Best Poster Award**
The 2nd International Conference on Nanoenergy and Nanosystems (NENS) 2016
- 2019 • **Best Poster Award**
The 4th International Conference on Nanoenergy and Nanosystems (NENS) 2019
-

PUBLICATION

1. U. Jeong Yang, **Jae Won Lee**, Jin Pyo Lee, Jeong Min Baik*, “Remarkable Output Power Enhancement of Sliding-Mode Triboelectric Nanogenerator through Direct Metal-to-Metal Contact with The Ground”, **Nano Energy**, Vol 57, pp. 293-299 (2019), **IF = 15.548**.
2. Jin Pyo Lee, † **Jae Won Lee**, † Bo-Kyung Yoon, Hee Jae Hwang, Sungwoo Jung, Katherine A. Kim, Dukhyun Choi, Changduk Yang, Jeong Min Baik*, “Boosting The Energy Conversion Efficiency of A Combined Triboelectric Nanogenerator-Capacitor”, **Nano Energy**, Vol. 56, pp. 571-580 (2019), (J. P. Lee, J. W. Lee are equally contributed in this work.) **IF = 15.548**.
3. Jin Pyo Lee, **Jae Won Lee**, Jeong Min Baik*, “The Progress of PVDF as a Functional Material for Triboelectric Nanogenerators and Self-Powered Sensors”, **Micromachines**, Vol 51, p. 532 (2018), **IF = 2.426**.
4. **Jae Won Lee**, Byeong Uk Ye, Zhong Lin Wang, Jong-Lam Lee, Jeong Min Baik*, “Highly-Sensitive and Highly-Correlative Flexible Motion Sensors Based on Asymmetric Piezotronic Effect”, **Nano Energy**, Vol. 51, pp. 185-191 (2018), **IF = 15.548**.
5. Jin Pyo Lee, Byeong Uk Ye, Kyeong Nam Kim, **Jae Won Lee**, Won Jun Choi, Jeong Min Baik*, “3D Printed Noise-Cancelling Triboelectric Nanogenerator”, **Nano Energy**, Vol. 38, pp. 377-384 (2017), **IF = 15.548**.
6. **Jae Won Lee**, Byeong Uk Ye, Jeong Min Baik*, “Research Update: Recent Progress in The Development of Effective Dielectrics for High-Output Triboelectric Nanogenerator”, **APL Materials**, Vol. 5, p. 073802 (2017), **IF = 4.296**.
7. **Jae Won Lee**, † Hye Jin Cho, † Jinsung Chun, Kyeong Nam Kim, Seongsu Kim, Chang Won Ahn, Ill Won Kim, Sang-Woo Kim, Changduk Yang*, Jeong Min Baik*, “Robust Nanogenerators Based on Graft Copolymers via Control of Dielectrics for Remarkable Output Power Enhancement”, **Science Advances**, Vol. 3, p. e1602902 (2017). **IF = 12.804**.
8. Jinsung Chun, Byeong Uk Ye, **Jae Won Lee**, Dukhyun Choi, Chong-Yun Kang, Sang-Woo Kim, Zhong Lin Wang, Jeong Min Baik*, “Boosted Output Performance of Triboelectric Nanogenerator via Electric Double Layer Effect”, **Nature Communications**, Vol. 7, p. 12985 (2016), **IF = 11.880**.
9. Hye Jin Lee, **Jae Won Lee**, Hee Jun Kim, Dae-Han Jung, Ki-Suk Lee, Sang Hyeon Kim, Dae-myeong Geum, Chang Zoo Kim, Won Jun Choi*, Jeong Min Baik*, “Optical Design of ZnO-Based Antireflective Layers for Enhanced GaAs Solar Cell Performance”, **Physical Chemistry**

Chemical Physics, Vol. 18, pp. 2906-2912 (2016), **IF = 3.906**.

10. Su-jin Kim, Yu Kyung Cho, Jeesoo Seok, Nam-Suk Lee, Byungrak Son, **Jae Won Lee**, Jeong Min Baik, Chongmok Lee, Youngmi Lee*, Myung Hwa Kim*, “Highly Branched RuO₂ Nanoneedles on Electrospun TiO₂ Nanofibers as an Efficient Electrocatalytic Platform”, **ACS Applied Materials & Interfaces**, Vol. 7, pp. 15321-15330 (2015), **IF = 8.456**.
11. Joonmo Park, **Jae Won Lee**, Byeong Uk Ye, Sung Hee Chun, Sang Hoon Joo, Hyunwoong Park, Heon Lee, Hu Young Jeong, Myung Hwa Kim*, Jeong Min Baik*, “Structural Evolution of Chemically-Driven RuO₂ Nanowires and 3-Dimensional Design for Photo-Catalytic Applications”, **Scientific Reports**, Vol. 5, p. 11933 (2015), **IF = 4.525**.
12. **Jae Won Lee**, Byeong Uk Ye, Dong-yeong Kim, Jong Kyu Kim, Jong Heo, Hu Young Jeong, Myung Hwa Kim, Won Jun Choi, Jeong Min Baik*, “ZnO Nanowire-Based Antireflective Coatings with Double-Nanotextured Surfaces”, **ACS Applied Materials & Interfaces**, Vol. 6, pp. 1375-1379 (2014), **IF = 8.456**.

PATENTS

1. Jeong Min Baik, **Jae Won Lee**, Jin Pyo Lee, U Jeong Yang, “Triboelectric Generator using Capacitor Structure.” Korea, Patent No. 10-2018-0174233 (2018).
2. Jeong Min Baik, **Jae Won Lee**, Jin Pyo Lee, U Jeong Yang, “Triboelectric Generator based on Elastic Body with Varying Restoring Force.” Korea, Patent No. 10-2018-0159040 (2018).
3. Jeong Min Baik, **Jae Won Lee**, Jin Pyo Lee, U Jeong Yang, “Self-Powered Health Care Sensor System.” Korea, Patent No. 10-2018-0123922 (2018).
4. **[Patent Registration]** Jeong Min Baik, Changduk Yang, Jae Won Lee, Hye Jin Cho, Sung Woo Jung, Jin Pyo Lee, “Charged Body Having Negative Electric Charge and Artificial Generator Comprising the Same.” Korea, Patent No. 10-2017-0085930 (2017), 10-19604470000 (2019).
5. **[Patent Registration]** Jeong Min Baik, **Jae Won Lee**, Jin Pyo Lee, Byeong Uk Ye, Duk Hyun Choi, Hee Jae Hwang, Wook Kim, “Method of Manufacturing Triboelectric Generator using 3D Printing.” Korea, Patent No. 10-2017-0030268 (2017), 10-19284280000 (2018).
6. Jeong Min Baik, Byeong Uk Ye, **Jae Won Lee**, Jin Pyo Lee, U Jeong Yang, “Triboelectric Generator.” Japan, Patent No. 2017-92857 (2017).

7. Jeong Min Baik, Byeong Uk Ye, **Jae Won Lee**, Jin Pyo Lee, U Jeong Yang, “Triboelectric Generator.” USA, Patent No. 15/589,091 (2017).
8. Jeong Min Baik, Byeong Uk Ye, **Jae Won Lee**, Jin Pyo Lee, U Jeong Yang, “Triboelectric Generator.” Korea, Patent No. 10-2016-0057218 (2016).
9. **[Patent Registration]** Jeong Min Baik, **Jae Won Lee**, Hee Jun Kim, “Hetero-Junction Metastructured Thin Film and Method for Manufacturing the Same.” Korea, Patent No. 10-2015-0189348 (2015), 10-17490670000 (2017).
10. Jeong Min Baik, Byeong Uk Ye, **Jae Won Lee**, “Method for Manufacturing Flexible GaN LED.” Korea, Patent No. 10-2015-0051985 (2015).
11. **[Patent Registration]** Jeong Min Baik, Byeong Uk Ye, **Jae Won Lee**, “Method for Forming Antireflection Coating Of Solar Cell.” Korea, Patent No. 10-2012-0138728 (2012), 1013639900000 (2014).

PRESENTATION

International Conference

1. International Conference on Nanoenergy and Nanosystems (NENS 2019), China, July 15 – 17, 2019. **Poster:** Fluorinated Polyimides Thin Films with Enhanced Charge Trapping Characteristics for High Output Power Nanogenerator.
2. The International Society for Optics and Photonics (SPIE Optics + Photonics 2018), USA, August 19 – 23, 2018. **Poster:** Fluorinated Polyimides Thin Films with Enhanced Charge Trapping Characteristics for High Output Power Nanogenerator.
3. International Conference on Nanogenerator and Piezotronics (NGPT 2018), Korea, May 8 – 11, 2018. **Oral:** Fluorinated Polyimides with Highly Efficient Charge Trapping Characteristics as an Effective Dielectric for High Output Triboelectric Nanogenerator.
4. 2018 Materials Research Society Spring Meeting & Exhibit (MRS 2018), USA, April 2 – 6, 2018. **Oral:** Fluorinated Polyimides with Highly Efficient Charge Trapping Characteristics as an Effective Dielectric for High Output Power Generation.
5. International Conference on Nanoenergy and Nanosystems (NENS 2017), China, October 21 – 23, 2017. **Poster:** Robust Nanogenerators Based on Graft Copolymers via Control of Dielectrics for Remarkable Output Power Enhancement.

6. 2017 Materials Research Society Spring Meeting & Exhibit (MRS 2017), USA, April 17 – 21, 2017. **Poster:** Fluorinated Polyimides with Highly Efficient Charge Trapping Characteristics as an Effective Dielectric for High Output Power generation.
7. International Conference on Electronic Materials and Nanotechnology for Green Environment (ENGE 2016), Korea, November 6 – 9, 2016. **Poster:** Effective Dielectrics of PVDF Graft Copolymer for Enhancing Triboelectric Nanogenerator.
8. The International Workshop on Piezoelectric Materials and Applications & Energy Conversion Materials and Devices 2016 (IWPMA&ECMD 2016), Korea, August 21 – 24, 2016. **Oral:** Effective Dielectric Constant of PVDF Graft Copolymer for Enhancing Triboelectric Nanogenerator.
9. International Conference on Nanoenergy and Nanosystems (NENS 2016), China, July 13 – 15, 2016. **Poster:** Effective Dielectric Property of PVDF Graft Copolymer for Enhancing Triboelectric Nanogenerator.
10. International Conference on Advanced Electromaterials (ICAE 2015), Korea, November 17 – 20, 2015. **Poster:** Polarization Dependence of Output Performance in p-type GaN Thin Films and Electroluminescence Properties in Vertical LEDs.
11. International Conference on Photochemistry (ICP 2015), Korea, June 28 – July 3, 2015. **Poster & Short Oral Presentation:** Structural Evolution of Chemically-Driven RuO₂ Nanowires and 3-Dimensional Design for Photocatalyst.
12. 2015 Materials Research Society Spring Meeting & Exhibit (MRS 2015), USA, April 6 – 10, 2015. **Poster:** Three-Dimensional RuO₂ Branched Au-TiO₂ Nanowire Heterostructures as Photostable and Efficient Photoelectrodes in Photo-Electrocatalytic Water Splitting.
13. International Conference on Nanoenergy and Nanosystems (NENS 2014), China, December 8 – 10, 2014. **Oral:** Polarization Dependence of Electroluminescence Properties and Output Voltage in Flexible N-face p-GaN Thin Films.
14. International Conference on Electronic Materials and Nanotechnology for Green Environment (ENGE 2014), Korea, November 16 – 19, 2014. **Poster:** Structural Evolution of Chemically-Driven RuO₂ Nanowires and 3-Dimensional Design for Photo-Catalytic Applications.
15. International Nanophotonics and Nanoenergy Conference (INPEC 2014), Korea, July 1 – 3, 2014. **Poster:** Polarization Dependence of Electroluminescence Properties and Output Voltage in Flexible N-Face p-GaN Thin Films.

Domestic Conference

1. The Korean Institute of Electrical and Electronic Material Engineers (KIEEME 2017), Korea, June 21 – 23. **Poster:** Output-Power Enhancement in Triboelectric Nanogenerators with PVDF Graft Copolymers through Dielectric Constant Control.
2. Spring Conference of the Korean Institute of Metals and Materials (KIM 2016), Korea, April 27 – 29, 2016. **Poster:** Effective Dielectrics of PVDF Graft Copolymer for Enhancing Triboelectric Nanogenerator.
3. 2016 Spring Conference of the Korean Institute of Metals and Materials (KIM 2016), Korea, April 27 – 29, 2016. **Poster:** Effective Dielectrics of PVDF Graft Copolymer for Enhancing Triboelectric Nanogenerator.
4. 2015 Fall Conference of the Korean Institute of Metals and Materials (KIM 2015), Korea, October 28 – 30, 2015. **Poster:** Structural Evolution of Chemically-Driven RuO₂ Nanowires and Three-Dimensional Design for Photocatalyst.
5. 2015 Spring Conference of the Korean Institute of Metals and Materials (KIM 2015), Korea, April 22 – 24, 2014. **Poster:** Polarization Dependence of Output Performance in Flexible GaN Thin Films and Electro-luminescence Properties in Vertical LEDs.
6. 2014 Spring Conference of the Korean Institute of Metals and Materials (KIM 2014), Korea, April 24 – 25, 2014. **Poster:** ZnO Nanowires-based Antireflective Surfaces with Hierarchical Morphologies.

SKILLS

- Technical:** Energy harvesting, Pressure sensitivity testing, Growth of metal oxide nanowire, Synthesis of ferroelectric nanoparticles, Electrospinning, Stretchable electrode, Biodegradable material, Bio-inspired materials, Photolithography photocatalyst, polymer synthesis, antireflection coating
- Laboratory** Material analysis (SEM, XRD, UPS), Processing equipment (E-beam evaporator, Sputter, Doctor blade, SLA/FDM based 3D printer, Filament extruder, Centrifugation, Langmuir Blodgett, Aligner), Measurement equipment (Oscilloscope, Current amplifier, Nanovoltmeter, Picoammeter, Electrometer, LCR meter, Bending tester, Folding tester, Pushing tester), Dielectric constant, PL, AFM
- Computer:** COMSOL simulation, Origin Lab, Rhinoceros, Microsoft office